Modelling Action Potential Firing Rate of Mouse Bladder Afferent Nerves in an Inflated Bladder Using Finite Element Analysis and Hodgkin-Huxley Models

Harley Ewing

Supervisor: Professor Mark Taylor

03 December 2020

Submitted to the College of Science and Engineering in partial fulfilment of the
requirements for the degree of Bachelor of Engineering (Mechanical) (Honours) / Master of
Engineering (Biomedical) at Flinders University - Adelaide Australia

Author’s Declaration

I certify that this work does not incorporate without acknowledgment any material previously submitted for a degree or diploma in any university; and that to the best of my knowledge and belief it does not contain any material previously published or written by another person except where due reference is made in the text.

Harley Ewing

June 2020

Acknowledgements

I’d like to thank my family and friends for being so patient for the duration of time I’ve taken to complete this thesis, and for the much longer amount of time taken to get here.

I’d like to thank my supervisor, Professor Mark Taylor. It was a difficult project with a steep learning curve and Mark helped me make sense of many difficult concepts and guided me through all the roadblocks along the way.

Finally I’d like to thank all the other university staff for helping make the final semester of my thesis study work. The advent of COVID-19 made the last semester less than ideal for any student in that period, but with their help a way was found through.

Abstract

This study modelled the action potential firing rate of mouse bladder afferent nerves for an inflated bladder using a finite element analysis and a Hodgkin-Huxley model. Pressure curve data was captured for *in vitro* mouse bladders using a multistage volumetric inflation. A 3D model replicating mouse bladder dimensions was constructed for the finite element model. Material properties and boundary conditions for the finite element model were assigned to emulate the *in vitro* bladder properties. The finite element model was performed in two stages, with the first stage capturing the displacement coordinates for the final volume, and the second stage capturing the viscoelastic stress response and staged volumetric inflation. Stress and displacement data were combined to recreate the *in vitro* pressure curves for finite element analysis model validation. A stimulus in the form of stress values from multiple nodes on the finite element model was applied to a modified Hodgkin-Huxley model. The Hodgkin-Huxley model generates a series of action potentials from which the firing rate is calculated. The stimulus stress values were input to the Hodgkin-Huxley model using both a linear relation and an exponential relation. Single nodes were examined showing that firing rate changes as a function of position for models where the stiffness changes as a function of position. Multiple node outputs were combined to simulate a receptor field, showing that firing rate increases as node count increases. Model validation was performed against existing firing rate data for a pressure volume curve. The exponentially modelled input was found to be a better fit for firing rate data validation.

Table of Contents

Table of Figures

List of Tables

1. Introduction

Computer modelling of neural outputs, which can be considered a subset of biological tissue modelling since neural outputs are a property of the material, is a relatively new field of study. The seminal work on modelling neural outputs was the research by Alan Hodgkin and Andrew Huxley in 1952. They performed research on squid giant axons using voltage clamp experiments and developed a model, now known as the Hodgkin-Huxley model, for action potentials as a function of the cumulative ion flux and capacitance across the cell membrane of the nerve. Their results garnered a Nobel prize.

Hodgkin and Huxley's model left room for future work with additional inputs (i.e. cell stimulus) to be modelled, including heat, chemical and mechanical inputs. Xu et al. (2008) used the work of Hodgkin and Huxley with good success modelling neural outputs for transdermal nociceptors (i.e. skin pain) as a function of thermal inputs. Xu and colleagues' research left significant work to be done for modelling nerve inputs as mechanical events.

This thesis aims to model the action potential firing rate of mouse bladder afferent nerves for an inflated bladder using finite element analysis and a modified Hodgkin-Huxley model. This research fills a gap in the field by modelling nerve mechanical events as a stimulus into a modified Hodgkin-Huxley model. Mouse bladders were chosen as the tissue type to be studied because of the readily available pressure volume curve experimental data and the simple mechanical environment that could be modelled from it. Neural output firing rate data of the distended mouse bladder is available from related previous research conducted on mice for model validation. A literature review is provided to give a broader understanding of the relevant research and how this research fits into that framework.

This research can be broadly divided into two parts. The first part models the mouse bladder undergoing volumetric inflation using the finite element method (FEM). The second part takes the stress values from the inflated bladder and feeds these values into a modified Hodgkin-Huxley model to model mouse bladder afferent nerve action potentials.

For the FEM model, preliminary pressure curve data was captured by Wade (Flinders University, 2019) for *in vitro* mouse bladders using a multistage volumetric inflation. A 3D model replicating mouse bladder dimensions was constructed and a FEM analysis was performed using this model. In the FEM model, material properties and boundary conditions were assigned to emulate the *in vitro* bladder properties. The FEM model was performed in two stages, with the first stage capturing the displacement coordinates for the final volume, and the second stage capturing the viscoelastic stress response and staged volumetric inflation. Stress and displacement data were combined to recreate the *in vitro* pressure curves for FEM analysis model validation. Stress data was captured at multiple time points from discrete positions on the bladder to be fed into the Hodgkin-Huxley model.

For the Hodgkin-Huxley model, stress values from multiple nodes on the FEM model were input to the Hodgkin-Huxley model. The results section of this research tests for firing rate against several variables. The output of the Hodgkin-Huxley model is the action potential firing rate as a function of stress. Stress values were input using both a linear relation and an exponential relation. Firing rate was tested against stress input for single nodes as a function of position. Firing rate was tested against stress input with increasing node counts. Model validation was performed against existing firing rate data for a pressure volume curve found in Daly (2014). A discussion of the results and conclusion is included at the end of the paper.

2. Literature Review

2.1 Bladder, Ureter, Urethra and Support Structures Anatomy

The bladder is a pressure vessel that stores urine ready for micturition at a later point in time. The gross anatomy of the bladder in mammals comprises the bladder with two ureters, which originate from the kidneys, emptying urine into the bladder. Inferior to the ureters is the urethra, which acts as the bladder outlet, emptying urine outside the body. The ureters and urethra enter the bladder close together in an area called the trigone. The urethra has an internal and external urethral sphincter to maintain bladder pressure (Marieb, 2012; Silverthorn, 2016; Widmaier, 2016). A diagram of the human bladder is shown in Figure 1.

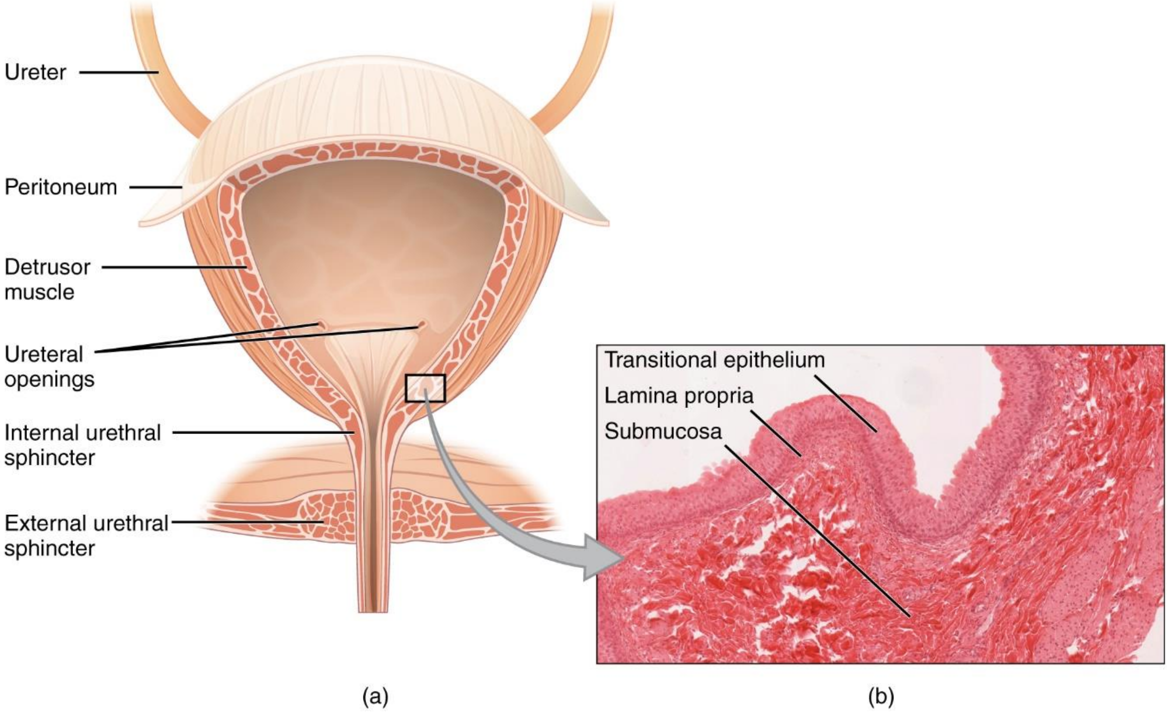

Figure 1 – (a) Human bladder anatomy and (b) histology of the bladder wall (Open Stax College, 2013)

The wall of the bladder consists mainly of the detrusor muscle. The bladder wall is composed of four layers; the urothelium, lamina propria, muscularis propria, and serosal layer. The urothelium is divided into three layers: the basal, intermediate, and superficial layers. The basal layer is comprised of small cuboidal cells. The intermediate layer cells are polygonal and can stretch and flatten. The superficial layer has large multinucleated cells that forms a protective layer for the bladder mucosa (Marieb, 2012).

The lamina propria has a basement membrane, which is a single layer of cells separating the epithelial layer from the lamina propria and which acts as a filtration barrier and supporting structure for the mucosal layer and separates it from the urothelium. It contains nerves, lymphatics, capillaries, elastic fibres, and a thin layer of smooth muscle called the muscularis mucosae. It has been suggested that the lamina propria acts as a capacitance layer for the bladder, signalling bladder compliance and enabling changes to the volume of bladder (Marieb, 2012).

The bladder wall contains interstitial cells of Cajal-like cells. It has been suggested that these cells may act as intermediary cells transducing nerve signals to detrusor smooth muscle cells (Drumm, 2014).

The detrusor muscle is the muscularis propria. It has three layers of muscles lying transverse to each other; the inner and outer longitudinal layers, and the intermediate circular layer. The layers consist of large, well defined bundles of muscle. The serosa covers the bladder with mesothelium (Marieb, 2012).

Innervation of the urinary bladder occurs from afferent and efferent nerves as shown in Figure 2. Sympathetic innervation of the bladder starts from spinal cord segments T10-L2, with preganglionic axons passing into primary sympathetic neurons in the inferior mesenteric ganglion and the ganglia of the pelvic plexus. The ganglia have postganglionic fibres that travel in the hypogastric and pelvic nerves of the bladder, where it is believed that the sympathetic activity relaxes the smooth muscle of the bladder (allowing urine accommodation) and causes the internal urethral sphincter to close (Purves, 2017).

Image removed due to copyright restriction.

Figure 2 – Innervation to the bladder, afferent nerves in green (Purves, 2017)

The afferent nerves' reflexes are supplied by mechanoreceptors in the bladder wall. These mechanoreceptors convey visceral afferent information to second order neurons in the dorsal horn of the spinal cord. These neurons also project into higher integrative centres in the periaqueductal grey of the midbrain (Purves, 2017).

The main function of the bladder afferent nerves is to signal bladder fullness to the brain. Fluid accumulation slowly stretches the bladder to a larger volume and applies pressure to the bladder wall (Marieb, 2012; Purves, 2017). The level of bladder fullness sensation is conveyed to the brain by tension-sensitive afferent nerves in the bladder wall (Morrison, 1999).

As the bladder nears capacity, sacral visceral motor outflow increases and thoraco-lumbar motor outflow decreases, which causes the bladder to contract and the internal sphincter to relax. Voluntary somatic motor innervation of the external urethral sphincter muscle holds urine in place ready for voluntary release (Purves, 2017).

Nerves transfer and store information across the body. Nerves consist of multiple neurons. The structure of a typical neuron, see Figure 3, is comprised of the presynaptic cell which has an axon (the signal conduction path) leading to the dendrite of a postsynaptic cell. The axon synapses onto a dendrite and conducts the signal (Purves, 2017; Reece, 2014).

Image removed due to copyright restriction.

Figure 3 – Nerve neurons and synapse (Reece, 2014)

Nerves transmit signals using action potentials. The neuron cell has a voltage potential across its membrane, known as the resting membrane potential; see Figure 4. The resting membrane potential is when the cell is at electrical rest, with no net movement of ions across the cell membrane, and is approximately -70 mV for neural cells. Neurons have gated channels in the membrane wall which can open or close in response to a stimulus (e.g. stretch) which can elicit changes in the membrane potential. When the stimulus raises the voltage high enough that it reaches the depolarisation threshold, many voltage gated ion channels open, triggering a large inflow of Na^+ that rapidly increases the voltage potential. The return of the cell's voltage to the resting membrane potential occurs by inactivation of the Na^+ channels and the opening of many K^+ channels, which increase K^+ efflux (Purves, 2017; Reece, 2014).

The nerve impulse (the action potential) travels from the axon hillock, along the axon to the synaptic terminal. The action impulse from the synapse signals the next synaptic cell to depolarise and continue the signal in a signalling cascade to the brain (Purves, 2017; Reece, 2014). The Hodgkin-Huxley model in this research models action potentials as a result of the bladder wall stress stimulus from the FEM model.

Image removed due to copyright restriction.

Figure 4 – Cell action potential (Reece, 2014)

There are multiple nerve types present in the bladder. Zagorodnyuk et al. (2007) classified the properties of major classes of mechano-sensory neurons projecting to the bladder by examining the effects of mechanical and chemical stimuli on guinea pig bladder afferents. They classified four types of bladder sensory neurons based on the difference in reaction to the stimuli and concluded that each functional class was likely to convey different types of information to the central nervous system. The different types of receptor are found in Table 1.

Table 1 – Summary table for properties of major classes of mechano-sensory neurons into bladder

Receptor Type	Activation Stimulus	Removal of Urothelium
Muscle mechanoreceptors	Stretch but not mucosal stroking with von Frey hairs, hypertonic saline, α, β-methylene ATP or capsaicin	No effect on stretch-induced firing
Muscle mechanoreceptors	Stretch, mucosal stroking with von Frey hairs, hypertonic saline, α, β-methylene ATP but not capsaicin	Reduction of stretch and stroking induced firing
Mucosal high-responding mechanoreceptors	Stretch-insensitive and activated by mucosal stroking with von Frey hairs, hypertonic saline, α, β-methylene ATP and capsaicin	Stroking induced firing significantly reduced
Mucosal low-responding mechanoreceptors	Stretch-insensitive and weakly activated by mucosal stroking with von Frey hairs, but not hypertonic saline, α, β-methylene ATP and capsaicin	Stroking induced firing reduced

Zagorodnyuk et al. showed that receptor types changed, both in what stimulus they were sensitive to, and their level of stimulus (i.e. low-responding versus high-responding). There were one to nine nerve receptor hotspots within a nerve field of $2.5 \pm 0.6\ mm^2$. This research represents the hotspots in a nerve field as multiple nodes on the bladder model, using the average of the numbers from Zagorodnyuk. The mucosal high and low-responding mechanoreceptors can be considered nociceptors (Zagorodnyjk 2008, Kendroud 2019).

Similar research was conducted by Xu and Gebhart (2008) on mouse bladders. They subjected an *in vitro* mouse bladder preparation to mechanical stimuli and found four different classes of afferent nerve: serosal, muscular, muscular/urothelial, and urothelial, with similar categorisations of activation stimulus as Zagorodnyuk. They found the lumbar splanchnic nerve contained mainly serosal and muscular afferents, while the pelvic nerve had all four classes. They found that these mechanosensitive afferents could detect a range of mechanical stimuli and each nerve class was tuned to detect a different type, magnitude and duration of stimulus. They classified the distribution of the classified nerve types which is reproduced in Figure 5.

Image removed due to copyright restriction.

Figure 5 – Nerve type and distribution on mouse bladder (Xu 2007)

De Wachter found that bladder sensations are not only the result of bladder distension and that other factors inside the bladder or bladder wall, e.g. central processing and/or cognitive manipulation, may have an important role. De Wachter also found that current methods to measure bladder sensations such as urodynamics, voiding diaries, forced diuresis, electrical stimulation and brain imaging may be sub-optimal since each factor is considered in isolation (De Wachter et al., 2012).

Zeng et al. found changes in mechanoreceptor afferent activity changed as a function of whether the bladder was obstructed or not, with peak contraction force and volume at peak contraction force both increasing dramatically but with the tension sensitivity of bladder mechanoreceptors and normalised pressure response much lower, resulting in a weaker afferent drive in adverse pathologies.

2.2 Bladder Mechanics and Models

Whole bladder properties during filling were examined by Damaser (1999, pp. 51-58). Damaser related bladder pressure volume filling to properties of the bladder that include elasticity, viscoelasticity, plastic deformation, bladder shape, mass and distension. The author modelled bladders as spheroids finding a small difference in the pressure-volume curve between it and a similarly modelled spherical bladder (i.e. a change in compliance was observed). It is shown that in most bladder models the viscous (rate dependent) properties of the bladder can be ignored in situations that mimic the physiological filling rate of the bladder, which is very slow. Conversely it is shown that studies that use medium and fast fill cystometry have pressure-dependent filling rates. Damaser made assumptions to simplify the bladder wall mechanical properties. The bladder was considered isotropic and homogenous in its wall material properties. Damaser used stress as a measure in place of force.

A spherical bladder shape has been assumed in many studies (Le Feber et al., 2004; Reigner, 1983; Tozeren, 1986; Watanabe et al., 1981).

Watanabe et al. (1981) used the law of Laplace ($p = \frac{2T}{r}$, where p = intravesical pressure, T = the mural tension and r = the radius of the spherical bladder) as a starting point to derive a new pressure volume equation. It was found when making use of the Mooney-Rivlin model that the Mooney-Rivlin material properties $c1$ and $c2$ are not constant.

Lotz et al. (2004) produced a model to predict the bladder shape based on changes in rectal and bladder filling. The model used CT scan data to produce the model mesh shapes. They used the assumption that for each domain of the bladder wall, the distance to a reference point, r, could be described as a linear function of two variables, the bladder and rectal volumes.

Argungu et al. (2015) developed three different models, each approaching a different aspect of the bladder. They modelled the mechano-sensitive response in afferent nerves by altering McKean's model of an excitable system and adding a stretch activated current. They made a quasi-linear viscoelastic model of the bladder wall. This model was successful in describing pressure as a function of time for increasing bladder volume. Lastly, they made a finite element method (FEM) model of the filling and emptying of a bladder. The model was limited in scope, being two dimensional only, but modelled the force during the filling and emptying phase. They identified a need to make a smooth walled bladder FEM model with forces on the bladder wall dependent on the nerve response.

A simple geometrical shape to represent the bladder geometry was used in other studies on the topic (El Sayed et al. 2007; Massey & Abrams 1985; Hilton & Stanton 1983; Reigner et al. 1983). Mouse bladders have very simple geometry and the elongated spheroid representation of the model geometry is closer to the tissue sample in shape than the spherical representation of a human bladder in other studies (Reis et al. 2011).

2.3 Bladder Elasticity and Viscoelasticity Models and Material Properties

The viscoelastic response of the bladder has been modelled in multiple studies as a function of strain.

Regneir et al. (1983) investigated the pressure-volume behaviour of the urinary bladder. They were able to model the viscoelastic properties by using a more complex *strain-energy* function, first used by Mooney (1940) and Rivlin (1948), and adding an exponential. They noted that voiding dynamics were likely related to some aspect of the filling phase and strain energy function but that had not been investigated at the time.

Fry (1999) found the extracellular matrix greatly influences the viscoelastic properties of the detrusor muscle and bladder. This work focused on obstructed bladder outflow to understand changes in contractile function of the bladder.

Van Mastrigt et al. (1978) found agreeance between a viscoelastic model that used three Maxwell elements (a spring and dashpot combination) with another purely elastic element in parallel. This related the viscoelastic response of the bladder wall with strain rate data obtained from pig urinary bladder strips. The expression they derived was based on a non-linear viscoelastic model with the elastic moduli depending exponentially on strain. The model incorporated three exponentials and a constant.

Barnes et al. (2015) measured the viscoelastic properties of porcine bladder tissue. Dynamic Mechanical Analysis was used on strips of tissue to test in the frequency range up to $10\ Hz$. Storage stiffness was found to be higher than loss stiffness. The results were tabulated for later use in computational modelling studies like this one.

The inflation of thick-walled, nonlinear viscoelastic spherical shells was examined by De Pascalis et al. (2015). Their model fit experimental data of the volumetric inflation of mouse bladders with a strain energy function. They developed a numerical technique to solve the nonlinear Volterra integral equation for a viscoelastic Mooney-Rivlin material, applying it to the inflation and deflation of a finite-thickness shell for a range of pressures.

Tozeren (1986) developed an analytical method to find the constitutive equations of the fibre material properties in a thick shell from the pressure volume curves obtained from experimental data.

2.4 Summary of key points and assumptions made for FEM and bladder models

- The bladder is assumed to be a prolate spheroid.
- Mechanoreceptor nerve distribution is evenly spaced over the bladder.
- Nerve type represented is simplified to a single universal mechanoreceptor.
- Analysis is performed on groups of nodes, representing the multiple hotspot inputs into a nerve.
- The input to the bladder is the volumetric displacement caused by urine influx.
- The Hodgkin-Huxley stimulus is the stress measured from the FEM bladder wall.
- Bladder material properties can be tuned to the model by starting with similar material properties and then holding all other model variables constant (tables of the material properties generated are listed in the methods section).

2.5 Finite Element Method

This is a short overview of the finite element method (FEM) as used in this research. Finite element method is a thoroughly researched topic and there are many good resources that expand on the topic (Logan, 2012; Kattan, 2008; etc.). These steps require significant effort on behalf of the researcher with a substantial proportion of time spent defining and troubleshooting each iteration of the problem (Spirka, 2010, p. 36).

The finite element method is a way to quantize a system and, using numerical techniques, give an approximate solution using simultaneous algebraic equations rather than solving using differential equations that an analytical model would give (Logan, 2012, p. 1; Pepper & Heinrich, 2017, p. 1). The FEM finds solutions to problems defined in geometrical space by dividing the geometrical domain into small elements with a central node (Pepper & Heinrich, 2017, p. 1) and finding approximate values to any unknowns at a discrete (finite) number set of points in the model continuum (Logan, 2012, p. 1).

The FEM can be divided into seven primary steps, according to Logan (2012, p. 8).

One, divide (discretise) the domain and select the element type and associated nodes. If the system is already discrete, like a frame or truss, then further division may not be needed, and the solution will be exact. If the system is continuous, like biological matter is, then the discretisation technique will become important and the solution will only be approximate (Kattan, 2008, p. 1). Modern FEM solvers represent the elements as triangles, tetrahedra, quadrilaterals or other more complex polygons (Pepper & Heinrich, 2017, p. 31), which can be used to build a three-dimensional mesh, which represents the physical geometry and some other aspects in the domain like fluids. A trade-off must be made between making the element small enough to give usable results and large enough to reduce the computational burden (Logan, 2012, p. 9).

Two, choose a displacement function for each element. This is defined using the nodal values of the element and can be a linear, quadratic, or cubic polynomial. These displacement functions are expressed in terms of nodal unknowns and are generally repeated for each element (Logan, 2012, p. 11).

Three, define the strain/displacement and stress/strain relationship equations necessary for deriving the equations for each element. E.g. for small strains we may relate strain $\varepsilon_x$and displacement u by $\varepsilon_x = \frac{du}{dx}$.

For defining material properties accurately, Hooke's law is often used to relate stress to strain, i.e. where stress = σ_x and the modulus of elasticity = E (Logan, 2012, p. 11)

$\sigma_x = E\varepsilon_x$.

Four, the element stiffness equations are written for each element in the domain (Kattan, 2008, p. 1) using either the work or energy method or alternatively using the method of weighted residuals (Logan, 2012, p. 12). These methods will produce the equations needed to describe the behaviour of each element. The element equations are written in matrix form as $\{f\} = [k]\{d\}$

where $\{f\}$ is the vector of element nodal forces, $[k]$ is the element stiffness matrix, and $\{d\}$ is the vector of unknown element nodal degrees of freedom or generalised displacements, n (Logan, 2012, p. 13).

Five, assemble the global stiffness matrix and apply boundary conditions to the system. The element nodal equations generated in step four are assembled into a global stiffness matrix in the form $\{F\} = [K]\{d\}$, which is a static solution where forces and displacements do not vary with time, where $\{F\}$ is the vector of global nodal forces, $[K]$ is the global stiffness matrix, and $\{d\}$ is the vector of known and unknown structure nodal degrees of freedom or generalised displacements (Logan, 2012, p. 14). To simplify the matrix, boundary conditions are applied (Logan, 2012, p. 14).

Six, solve the system of equations by partitioning the global stiffness matrix. This gives rise to further equations which are solved by Gaussian elimination (Kattan, 2008, p. 1). This gives solutions for the displacement of the nodes (Logan, 2012, p. 8).

Seven, solve for information like element forces, stresses, and strains (Kattan, 2008, p. 1; Logan, 2012, p. 14). These can be derived from the displacement solutions previously obtained in step six using assigned material properties.

Lastly, the results are interpreted. Troubleshooting and reiteration of the problem are performed after results are obtained.

2.6 Hodgkin-Huxley Model

The original Hodgkin-Huxley model describes the nerve impulse moving in a squid giant axon. Hodgkin and Huxley modelled the action potential of the nerve as a series of currents moving across the cell membrane.

A very brief description of the Hodgkin-Huxley model follows, as described by Cronin (1987).

The Hodgkin-Huxley equations describe the action potentials along the axon by modelling variations of the cell membrane potentials and ion currents. The model is a quantitative description of the data gained from initial experimentation, which was obtained by voltage-clamp experiments. These experiments provide a set of conditions that are not an exact replica of in-vivo conditions. In the experiments the membrane potential is constant and the ionic currents are a function of time only, which is a simplification of in-vivo conditions.

The voltage-clamp experiments can determine the capacitance of the membrane per unit area (C_M) by the following equation: (Cronin, 1987, p. 23)

$$I = C_M \frac{\delta V}{\delta t} + I_i \qquad (1)$$

Where $I = total\ current$

$$C_m = membrane\ capacitance$$

$$\frac{\delta V}{\delta t} = change\ in\ V\ w.r.t.time$$

$$I_i = ionic\ current$$

The voltage-clamp experiment allows for V to be held constant and when this condition is met, $\frac{\delta V}{\delta t} = 0$. This gives a capacitance current of zero and the total current across the membrane, I will equal the ionic current I_i. I.e.

$$I = I_i$$

Since I can be measured in the voltage-clamp experiment then the ionic current can also be measured.

The contribution of different ions to the current across the membrane can be measured with the Nernst equation and further experimentation. A nerve cell (axon) has intracellular fluid that consists of sodium (Na), chloride (Cl), and potassium (K). The concentration of Na inside the axon is approximately 1/10 the concentration of Na outside the axon. The concentration of K outside the axon is approximately 1/5 the concentration inside the axon. The differences in concentration provide an electromotive force (emf) equivalent to the Nernst formula:

$$E_{ion} = \frac{RT}{F} \ln \frac{C_i}{C_o}$$

where C_i and C_o are the inside and outside of the axon ionic concentrations, R is the gas constant ($R = 8.31432 \times \frac{10^7 erg}{°C}\ per\ mole$), T is the temperature in Kelvin, and F is Avogadro's number ($F = 6.022 \times 10^{23}\ mol^{-1}$). This is used to verify the influx and efflux of Na and K currents across the membrane. Further experiments are performed to show that

$$I_i(t) = I_{Na}(t) + I_K(t)$$

and

$$I_i{}'(t) = I'_{Na}(t) + I'_K(t)$$

where $I_{Na}(t)$ and $I'_{Na}(t)$ are the Na currents and $I_K(t)$ and $I'_K(t)$ are the K currents. More data and assumptions are collected and made respectively to show the permeability of the membrane to Na and K.

$$membrane\ permeability = g_{ion} = \frac{I_{ion}}{E - E_{ion}}$$

where E is the equilibrium potential and $-E_{ion}$ is the emf of the ions.

After considerable further work Hodgkin and Huxley deduced that the final equations would take the form:

$$\frac{dV}{dt} = F(t, V, g_{Na}, g_K)$$

$$\frac{dg_{Na}}{dt} = G(t, V, g_{Na}, g_K)$$

$$\frac{dg_K}{dt} = H(t, V, g_{Na}, g_K)$$

The final Hodgkin-Huxley equations start with the summation of the Na and K currents and add a leakage current.

$$I_i = I_{Na} + I_K + I_l \qquad (2)$$

Equation 2 is substituted into equation 1.

$$I = C_M \frac{dV}{dt} + I_{Na} + I_K + I_l \qquad (3)$$

In words, the total current is equal to the sum of the capacitance current and ionic currents.

The currents are considered separately and have no influence on each other.

$$I_{Na} = g_{Na}(E - E_{Na}) \qquad (4)$$

$$I_K = g_K(E - E_K) \qquad (5)$$

which are the sodium and potassium currents respectively.

The leakage current can be represented by a positive constant, $\bar{g}_l$, and E the equilibrium potential for the ions.

$$I_l = \bar{g}_l(E - E_l) \qquad (6)$$

Substituting equations 4, 5 and 6 into equation 3.

$$I = C_M \frac{dV}{dt} + g_{Na}(E - E_{Na}) + g_K(E - E_K) + \bar{g}_l(E - E_l) \qquad (7)$$

Rewriting the electromotive forces in terms of voltage.

$$E - E_{Na} = V - V_{Na} \qquad (8)$$

$$E - E_K = V - V_K \qquad (9)$$

$$E - E_l = V - V_l \qquad (10)$$

Substituting equations 8, 9 and 10 into equation 7 and solving for $\frac{dV}{dt}$.

$$\frac{dV}{dt} = \frac{1}{C_M}[I - g_{Na}(V - V_{Na}) - g_K(V - V_K) - \bar{g}_l(V - V_l)] \qquad (11)$$

Equation 11 is the first version of the Hodgkin-Huxley equations. Equations 12, 13, 14 and 15 are the final versions of the Hodgkin-Huxley equations, which take into account other factors:

$$\frac{dV}{dt} = \frac{1}{C_M}[I - \bar{g}_{Na}m^3(V - V_{Na}) - \bar{g}_K n^4(V - V_K) - \bar{g}_l(V - V_l)] \qquad (12)$$

$$\frac{dm}{dt} = \alpha_m(1 - m) - \beta_m m \qquad (13)$$

$$\frac{dh}{dt} = \alpha_h(1 - h) - \beta_h h \qquad (14)$$

$$\frac{dn}{dt} = \alpha_n(1 - n) - \beta_n n \qquad (15)$$

where $\alpha_m, \beta_m, \alpha_h, \beta_h$ are non-negative functions of V, and dependent variables m and h are the activation and inactivation variables.

The Hodgkin-Huxley model used in this research is a derivative of equations 12 through 15. Xu et al. (2008) modelled the stimulation current as the summation of currents due to heat, chemical and mechanical events. I.e.

$$I_{st} = I_{heat} + I_{chem} + I_{mech}$$

The current for the mechanically gated channel was modelled as a function of the stress at the nociceptor, σ_n, and a mechanical pain threshold, $\sigma_t = 0.2\ MPa$.

$$I_{mech} = f_m(\sigma_n, \sigma_t)$$

In this research both heat and chemical stimuli are ignored, reducing the stimulation current to

$$I_{st} = I_{mech}$$

Xu assumed the mechanical currents were modelled with a linear relationship between the stimuli and the generated currents.

$$I_{mech} = \frac{C_m(\sigma_n - \sigma_t)}{\sigma_t}$$

where $C_m = 20\mu A/cm^2$.

The mechanical currents in this research are modelled with both a direct linear relationship, $I_{mech} = c\sigma_n$, and an exponential relationship, $I_{mech} = c(\mathrm{e}^{\sigma_n})$, where c is a constant.

Modelling the mechanical current relationship as an exponential is similar to Xu's approach to modelling the heat currents, which were modelled as

$$I_{heat} = C_{h1}\left(\mathrm{e}^{\frac{(T_n - T_{t)}/T_t}{C_{h2}}} + C_{h3}\right) + I_{shift} \times H(T_n - T_t)$$

which in simplified form is $I_{heat} = c_1(\mathrm{e}^{T_n}) + c_2$,

Additional changes were incorporated from Shapiro and Lenherr (1972, p. 1147) who improved low frequency neuron firing by determining the rate of repolarisation as a function of a time constant for potassium activity, T_n. The time constant was multiplied by a voltage dependent function.

$$T_n^* = 1/\gamma T_n$$

Where T_n^* is the new Hodgkin-Huxley function and γ is a function of voltage and varies linearly with voltage such that

$$\gamma = \frac{1}{\gamma_0} - \frac{\left(1 - \frac{1}{\gamma_0}\right)V}{115}$$

When $V = 0, \gamma = 1/\gamma_0$ and when $V = V_{Na} = -115mv, \gamma = 1$. For $\gamma_0 = 1$, the equations revert back to the unmodified Hodgkin-Huxley equations.

2.7 Further research on Hodgkin-Huxley model

The original Hodgkin-Huxley (1952) paper described the action potential of a squid giant neuron by modelling the ionic current flux and capacitance of the cell membrane. Several authors have extended research in this field.

Xu et al. (2008) modelled skin thermal pain using the Hodgkin-Huxley model. Thermal pain was modelled as an exponential plus constant input, while mechanical pain stimulus was assumed to be a direct linear relation.

Other papers have modelled sensory information using the Hodgkin-Huxley model (Miftakhov and Wingate, 1996; Nemoto et al., 1975; Takeuchi et al., 2001; Torkkeli and French, 2002).

Pawluk and Howe (1997) used the mechanical displacement of the skin as the input to the Hodgkin-Huxley model, with a skin displacement function modelled as first and second order differentials.

3. Methodology and Experiment Details

3.1 *In vitro* pressure data from mouse bladder

The volume pressure data was obtained from Tracy Wade (personal communication, June 2019). Four sets of data were obtained that show the multistage inflation of a mouse bladder with isotonic solution while measuring the pressure response. Each bladder undergoes an initial basal infusion of $100\ \mu L$ of isotonic solution at a rate of $30\ \mu L/min$ followed by a $10\ min$ rest period. This is followed by a $50\ \mu L$ infusion at a rate of $30\ \mu L/min$ followed by a $10\ min$ rest period. This is repeated until the experiment ends. This bladder inflation had 18 infusions and a final infusion until the bladder burst. A graphical depiction of the data set used is shown in Figure 6.

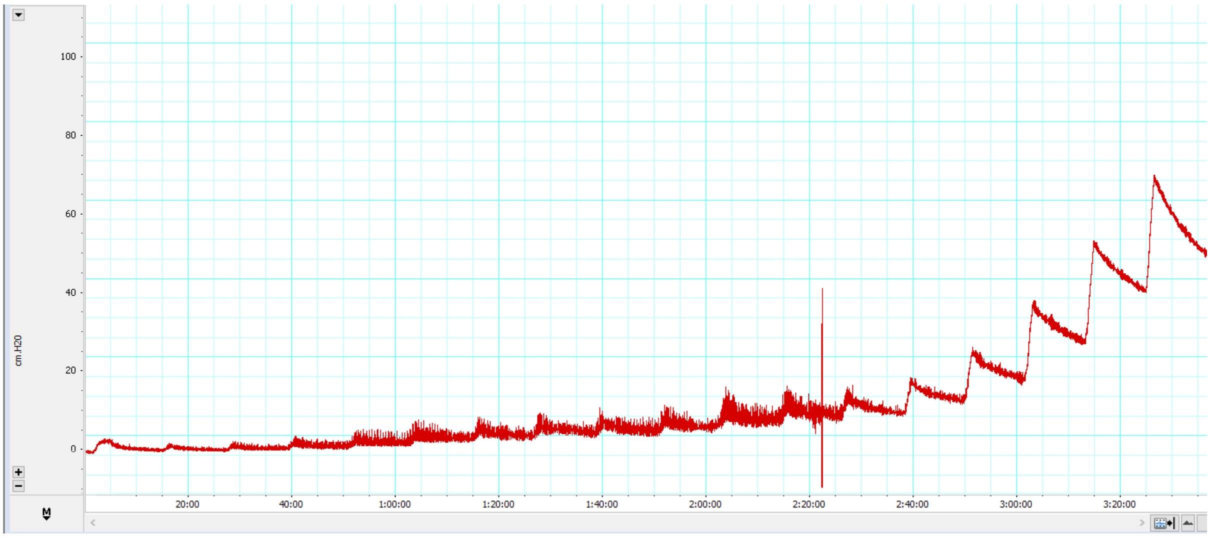

Figure 6 – LabView pressure curve for mouse bladder inflation

The initial bladder volume and subsequent bladder volumes after each infusion is shown in Table 7 (see Appendix 4).

The peak pressure value was taken as 63.7 $cmH2O = 0.00637\ MPa\ at\ 1026\ \mu L$. This data was used for the load source and defines the volume and its pressure at that volume. Later, the stress data is read from the final FEM analysis and, using a thin wall pressure vessel analysis, is matched back against this initial pressure curve to confirm that the pressure curves match.

A second source of *in vitro* data was taken from Daly et al. (2014), who inflated mouse bladders with saline and measured the volume of fluid injected in a ramp distension while measuring the pressure response up to a maximum of $50\ mmHg = 0.00667\ MPa\ at\ 420\ \mu L$. The Daly experiment also measured the neuronal firing rate of the mechanoreceptors of the bladder while undergoing inflation. These results are shown in Figure 7. Of note is the much smaller time frame over which the total volume was injected which leads to a higher pressure for a smaller volume due to the viscoelastic response of the bladder material. A model was made to match the properties of these data as a validation of the firing rate for the pressure volume relationship recorded in Daly's research.

Image removed due to copyright restriction.

Figure 7 – Ramp distension to 50 mmHg (Daly 2014)

3.2 Modelling mouse bladder geometry

The mouse bladder is a symmetrical prolate spheroid with two entering ureters and one exiting urethra. The 3D bladder model was generated using measurement data for partially empty (residual fluid is present) bladders taken from a cohort of 4 mice (3 male, 1 female).

The bladders were excised and measured. Both the external dimensions and the wall thickness were measured. The results are tabulated in Table 2. The tabulated results are similar to dimensions found by Reis et al. (2011).

Table 2 – tabulated dimensions for 4 adult mice

Bladder Number	Sex	Major Axis (mm)	Minor Axis (mm)	Wall Thickness (mm)
1	M	6.40	4.60	0.026
2	M	6.60	4.42	0.027
3	F	7.25	4.96	0.021
4	M	6.71	4.58	0.040
Mean Diameters		6.74	4.64	
Mean Radius		3.37	2.32	
Mean Wall Thickness (mm)				0.027

The initial 3D model was made to the mean dimensions. The model was constructed in Autodesk Inventor Professional and saved as a parametric file. Simplifications were made to reduce model complexity, with the ureters and urethra being removed for the analysis. This file was then opened in the open source meshing software Gmsh for meshing. The mesh element type chosen used the default surface type of tet4. The mesh density was chosen so that it was high enough that later node selection had enough node points to choose from. The bladder mesh is shown in Figure 8. This bladder has 958 faces and 481 nodes.

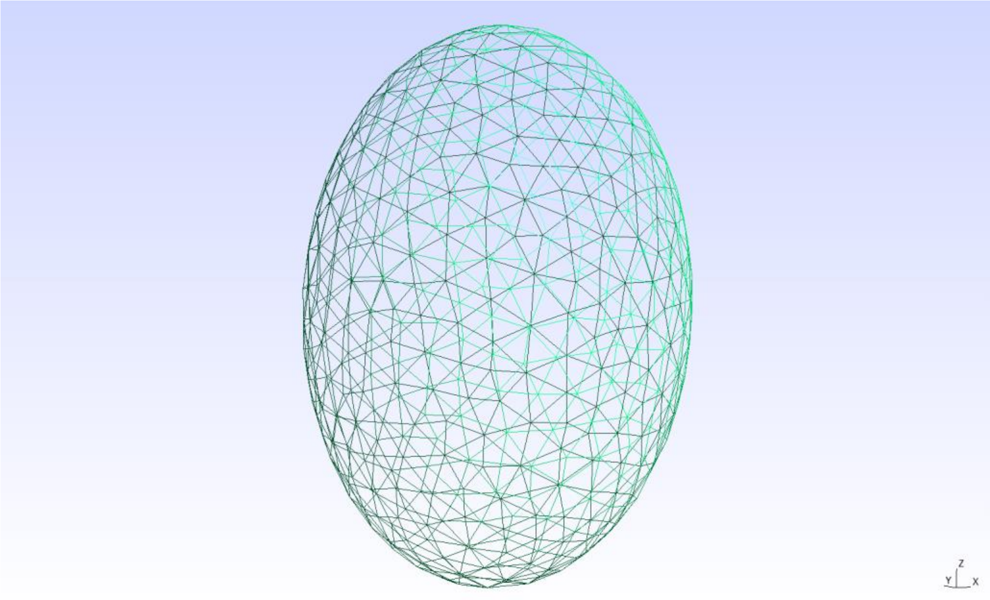

Figure 8 – Mouse bladder meshing as shown in GMSH

In a mouse bladder there are ureterovesical valves on the ureters to prevent vesicoureteral reflux (backflow) and a urethral sphincter to control micturition events. The ureters and urethra were excluded from the model geometry because they undergo no pressure changes from the contraction of the detrusor muscle during micturition due to the valves.

3.3 Finite Element Analysis Software - FEBio

The software used for the FEM section of this research is the open source package FEBio. The FEBio software suite is used for the processes described henceforth. FEBio consists of three different programs: PreView, FEBio, and PostView. The researcher needs to generate the geometry and FEM mesh, define the material properties and other boundary conditions, then use FEBio to solve for the given parameters.

PreView is a graphical user interface (GUI) used to generate geometry and meshes, and set up the boundary conditions, and which generates an input file that is processed in the FEBio program.

FEBio is the FEM solver and takes either a hand coded file or a file output from PreView which contains code that describes the model geometry (mesh), all boundary conditions, material properties, forces, displacements, etc., and processes this code using the FEM to generate an output file. The output file can then be opened in the third binary, called PostView.

Postview is a GUI that allows the user to visualise the final FEM model, inspect the data, and output the final data ready for further analysis. This stage is often used to feedback changes into the original PreView model to move the iterated output data closer to the desired result.

Within FEBio there are two approaches to the problem: using either a dynamic model with fluid structure interactions to solve for stress; or using a static model, with pressure and displacement to solve for stress.

The aim of the FEM model is to create a simulation that closely replicates the inputs, which are the injected fluid volumes, and output, which is the pressure curve, of the *in vitro* experiment. The model must closely replicate the staged filling of the *in vitro* experiment, with model parameters that replicate the properties of the mouse bladder and give a final pressure output with a close match to the data from Figure 6.

During the research project, considerable time was spent on a dynamic model with fluid structure interactions. A dynamic FEM model uses equations relating force and displacement that vary with time. The equation in step five in the FEM explanation is replaced with $\{F(t)\} = [M]\{\ddot{\delta}\} + [C]\{\dot{\delta}\} + [K]\{\delta\}$, where $[M]$ is the global mass matrix, $[C]$ is the global damping matrix, $\ddot{\delta}$ is the second derivative of the nodal displacement vector with respect to time, and $\dot{\delta}$ is the first derivative of the nodal displacement vector with respect to time (Logan, 2012, p. 14).

The bladder model was inflated by a fluid domain; see Figure 9. The model was constructed as a single stage FEM analysis. The model consisted of a bladder with urine inlet and exit. In the model constructed, model boundary conditions represented the urethra as the bladder inlet and the ureters as blocked from flow (by increasing the exit flow resistance to a very high level). The model was fixed in space at the rim of the urethra, allowing the whole model to react as a result of the fluid influx. The material properties were approximately the same starting values as presented later in this research. The model solved for bladder wall displacement as a function of the fluid accumulation, with stress readings taken directly from the bladder wall.

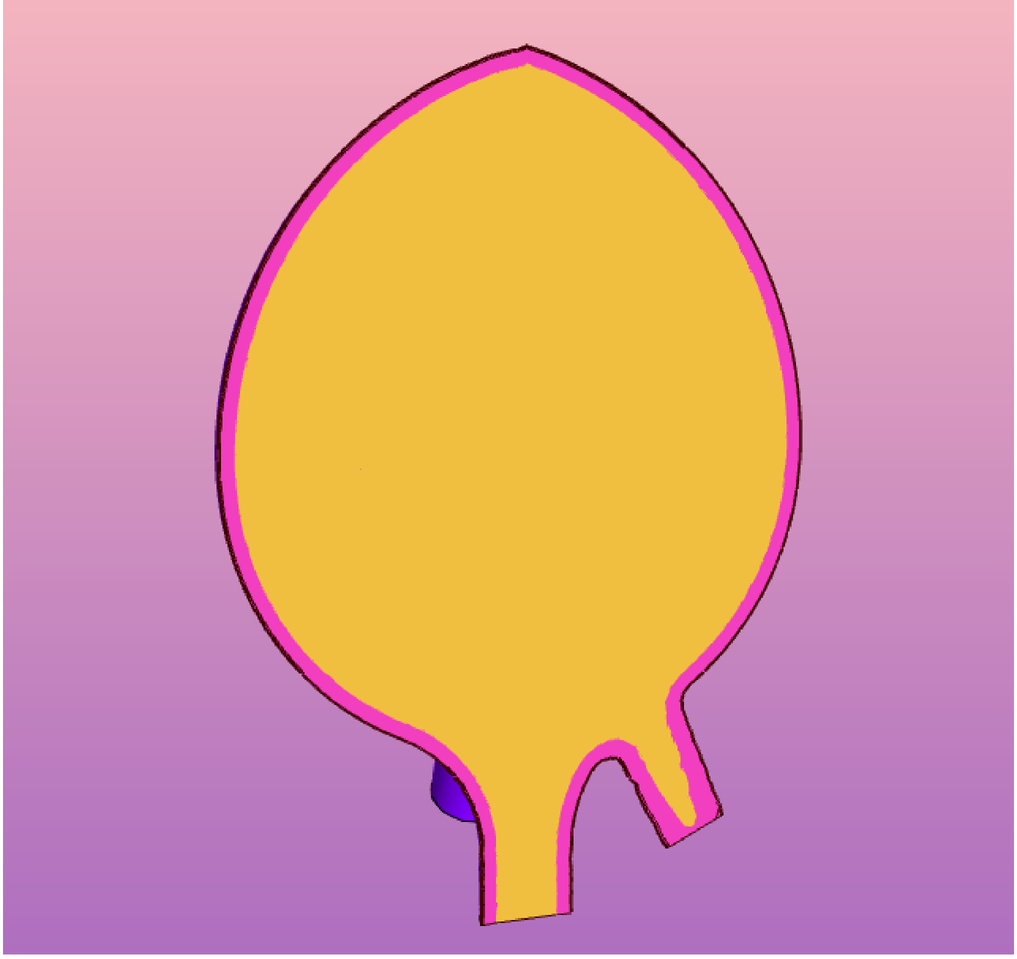

Figure 9 – Fluid structure interaction bladder model, fluid domain shown in yellow. The cross-section bisects the urethra in the centre and a ureter to its right.

This model presented too many complexities to be completed on time and took up too much computing resources. On a 4 GHz quad core PC with 32 GB of system memory and a fast SSD drive, the computation times were in the order of days. When performing iterative changes each full FEM computation would take up to 48 hours, restricting iterative changes to that time interval. The dynamic model did allow a stress and pressure solution to be read directly from the single model. With some optimisations (e.g. computing on a small slice of a symmetric model) the model may have come down in computation time. In the end it was a non-trivial problem that would have taken far too much time to continue on that path.

The dynamic model was abandoned in favour of a two part linear and dynamic model, respectively. The aim of the first part of the static FEM model was to replicate the bladder properties and to expand it by an internal fixed pressure equivalent to the end pressure on the *in vitro* model, to the maximum volume of the *in vitro* model. The final displacement of the bladder wall from the first part is then fed into the second part of the model. This replicates the filling and rest periods of the *in vitro* model by inflating the model using a load curve to control the rate of inflation to the fixed volumes represented in the *in vitro* model. Lastly, the stress relaxation response of the bladder wall is measured from the bladder model wall

This second method represented a considerable simplification of the FEM model, saving substantial time.

3.4 FEBio model loading and boundary conditions

The bladder stress data is generated from the finite element method model. The method to generate the FEM model followed a series of steps in two distinct stages. The first stage used a linear model with pressure input on the interior surface of the mesh to inflate the bladder to the same volume as the volume pressure data in Table 7 (see Appendix 4).

The *in vitro* data from Wade gives two pieces of information; the volume injected into the bladder and the bladder pressure associated with the fluid injection, i.e. a volume pressure curve. Using the predefined volume pressure curve with the model geometry defined from measurements, the only variables are material properties.

The steps used to inflate the bladder to the final volume were as follows: import the geometry mesh, extrude the mesh to the desired bladder thickness, apply a pressure displacement to the inner bladder surface, apply material properties to the mesh, check the final volume of the mesh, and make changes to the material properties of the model to get closer to the final *in vitro* volume. The last two steps form a recursive loop with material properties adjusted until the FEM model volume matches the final *in vitro* volume.

The algorithm for volume matching is:

1. Run the initial FEM analysis.

2. Check the FEM model final volume against the *in vitro* final volume.

3. Alter the material variables to adjust the FEM model final volume.

5. Repeat from step 2 until the volumes for each of the data sets are within 0.1% of the final *in vitro* volume.

The final target volume for the Wade data is $1026\ \mu L$ at $63.7\ cmH2O = 0.00637\ MPa$.

The final target volume for the Daly data is 420 μL at $50\ mmHg = 0.00667\ MPa$.

The mesh generated by Gmsh is imported into PreView and structural analysis is chosen. This is a static analysis. At this point the mesh has no thickness and is selected and extruded to the measured wall thickness of a mouse bladder, $0.27\ mm$ from Table 1.

Using the peak pressure value from the *in vitro* data, a linear pressure load of $0.00637\ MPa$ for the Wade model and $0.00667\ MPa$ for the Daly model was applied to the inner surface of the mesh; see Figure 10.

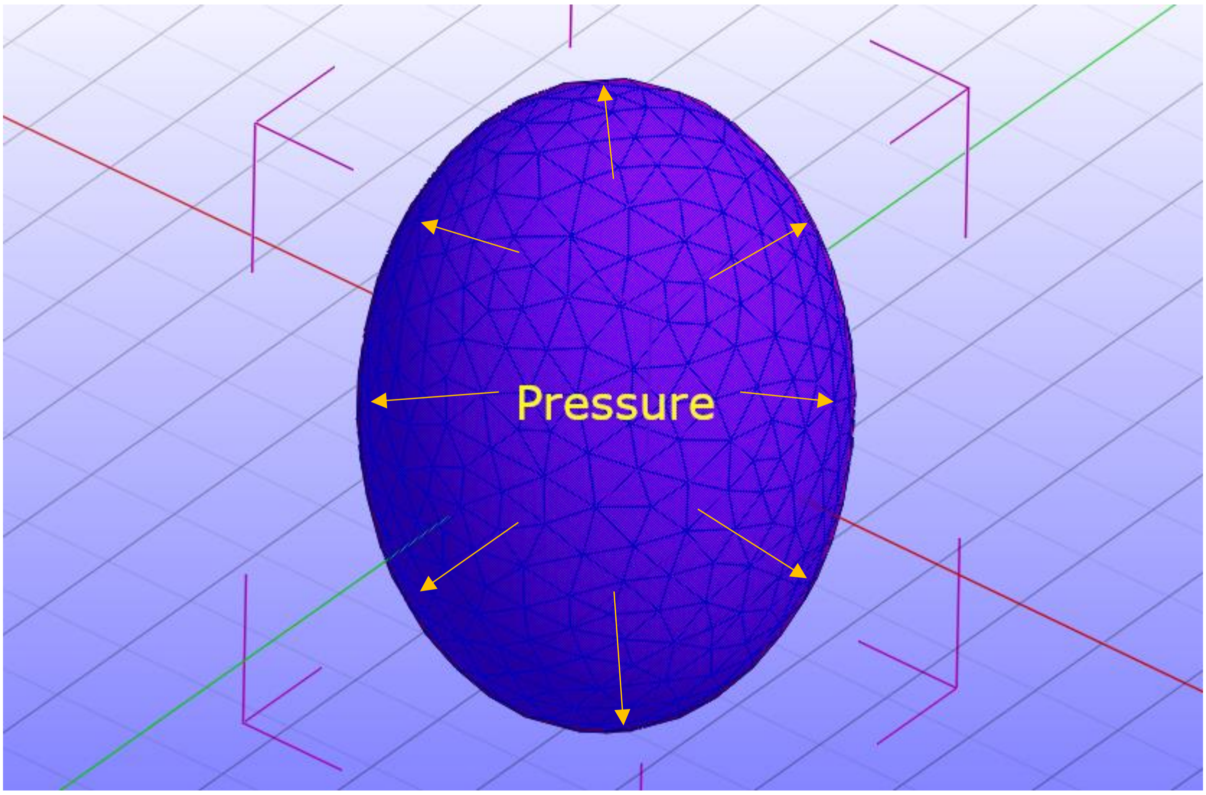

Figure 10 – Inner bladder surface pressure assignment in PreView.

The boundary conditions for the movement of the mesh in space were defined by restricting two points on the mesh. This uses the Fixed Displacement function. Nodes on the centre top and bottom of the mesh were chosen.

To isolate the elastic pressure response from inflating the bladder, an appropriate time frame was chosen that removes any influence of the viscoelastic response on the tissue. The minimum step size chosen was $1\ s$ and the time steps chosen was 100000, giving a total time of $100000\ s$, which is several orders of magnitude outside of the relaxation response properties (the maximum relaxation time is variable <t3> = 100 *s*, shown in Table 6 below). The maximum step size chosen was $500\ s$ to reduce the calculation burden. This allows FEBio to dynamically change the calculation interval up to 500 *s* based how large the previous changes in the model were, i.e. if the changes in the model between calculations are very small, it increases the time step size. Run time for this part of the model was approximately 10 minutes. Excluding the viscoelastic response is not strictly necessary since the static nature of the model should remove the inertial effects of the material, i.e. the viscoelastic properties, and the end goal is finding the displacement of each node for a fixed volume.

Part of the research aims to model the viscoelastic properties of the mouse bladder in the FEM model. To achieve this the FEM analysis was divided into two stages. In the first stage, the model undergoes a fixed pressure inflation to a finite volume, matching the model to the *in vitro* bladder maximum pressure and final volume. With a fixed pressure inflation, FEM analysis cannot capture the viscoelastic response since the pressure on the material is constant and the model slowly increases volume. The second stage measures the viscoelastic response from a fixed volume. By using the same material properties and using a fixed displacement of the bladder to the same final volume (using the data from the final model coordinates from the first stage of the analysis) the viscoelastic response is measured.

3.5 Material Properties

Material properties were applied to the bladder. The main material in the bladder is the detrusor muscle. The detrusor muscle displays viscoelastic properties. The elastic and viscoelastic material properties are separately defined within PreView. The elastic properties were defined as a Mooney-Rivlin material. The viscoelastic properties were defined as an uncoupled viscoelastic material. This is consistent with other studies that have used these properties (Spirka, 2010).

3.5.1 Elastic Material Definition

The Mooney-Rivlin material is a hyperelastic material type with uncoupled deviatoric and volumetric behaviour. FEBio variable descriptions are shown in Table 3.

Table 3 – FEBio Mooney-Rivlin elastic material variables

Variable name	Variable description
<density>	Density of rigid body
<c1>	Coefficient of first invariant term
<c2>	Coefficient of second invariant term
<k>	Bulk modulus

The initial density, c1, c2 and bulk modulus were taken from a similar tissue definition (UCL Medical Physics and Biomedical Engineering, 2015, September 23) and are seen in Table 4, second column. The final properties after fitting are seen in Table 4, third column.

Table 4 – FEBio Mooney-Rivlin elastic material variables. Column 2 shows the values before fitting. Columns 3 and 4 shows the values after fitting for the two different models.

Variable name	Variable initial value	Wade variable value after fitting	Daly variable value after fitting
<density>	1.002e-06	1.002e-06	1.002e-06
<c1>	0.165	0.0656	0.0697
<c2>	0	0	0
<k>	16.39	16.39	16.39

3.5.2 Uncoupled Viscoelastic Material Definition

The uncoupled viscoelastic material produces a viscoelastic response for the deviatoric stress response. The FEBio variable descriptions are shown in Table 5.

Table 5 – FEBio uncoupled viscoelastic material variables

Variable name	Variable description
<t1>-<t6>	Relaxation times
<g1>-<g6>	Viscoelastic coefficients
<elastic>	Elastic component (must be an uncoupled elastic solid)

The viscoelastic response is defined by the relaxation time variables. These were modelled in accordance with models by van Mastrigt et al. (1978) with three exponential values and a constant. The viscoelastic portion of the material was initially defined with properties as seen in Table 6 second column, and final properties after fitting as seen in Table 6, third column.

Table 6 – FEBio uncoupled viscoelastic material variables

Variable name	Wade and Daly variables initial value	Wade and Daly variables value after fitting
<t1>	1	1
<t2>	10	10
<t3>	100	100
<g1>-<g3>	0.18	0.9

These material properties represent the initial loading conditions. They are variables and their values changed as the model is fit to the *in vitro* data. The material properties were tuned for both the Wade model and for the Daly model. The material properties stayed largely the same, with only the $c1$ variable from the elastic property in Table 4, differing by approximately 6% between the models. The $c1$ variable has a direct correlation to the overall stress within the material and changing this value adjusts the magnitude of the final pressure curve.

3.6 First Stage FEM Analysis

The first stage analysis was run, and the results were obtained from this stage. The previously mentioned loop was iterated through, with the value of $c1$ altered to change the inflation volume to match the infusion volume. The bladder inflation from pressure for the Wade model is shown at the initial and final time steps in Figures 11 and 12, respectively.

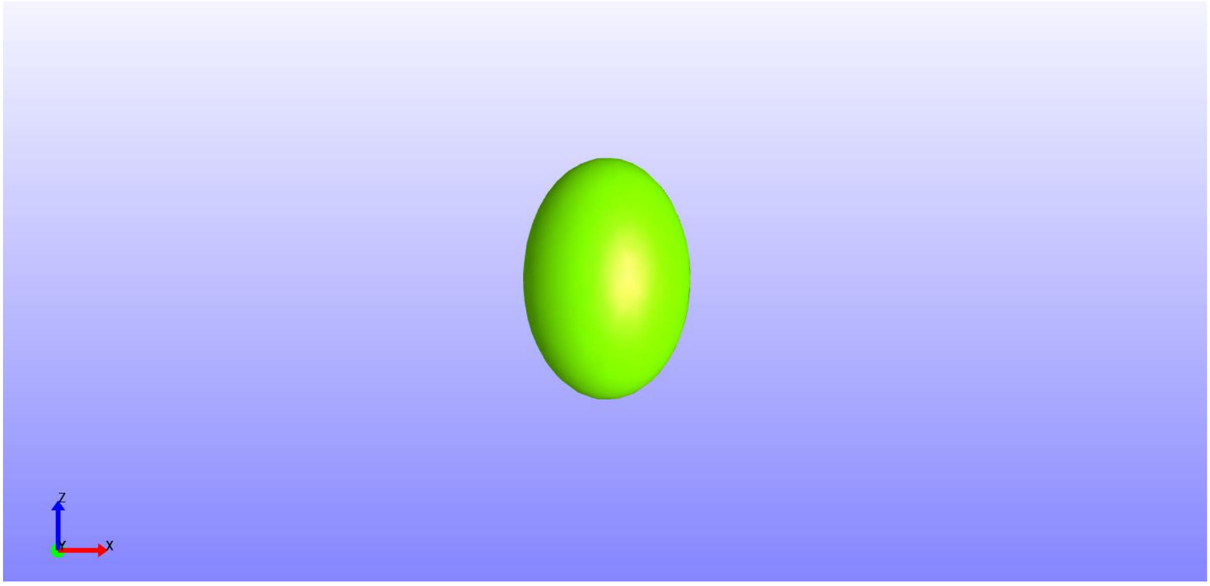

Figure 11 – Bladder mesh with no inflation at time t = 0 s

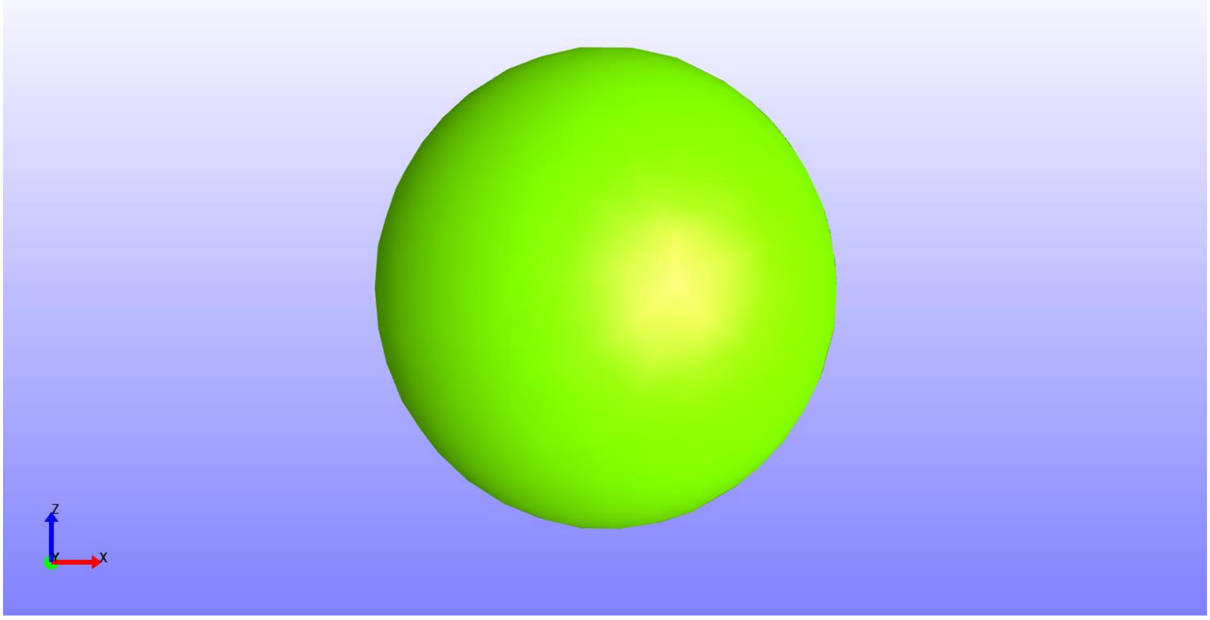

Figure 12 – Bladder mesh with maximum inflation at time t = 12700 s

3.7 Second Stage FEM Analysis

The second stage of the analysis uses a hand coded file and several code portions generated using MATLAB. This stage of the analysis uses a fixed displacement to the previously calculated final volumes instead of a pressure displacement. This allows the FEM software to calculate the viscoelastic pressure response for each stage of the inflation.

The setup of this file started by replicating all the previous properties and boundary conditions but replacing the singular fixed pressure inflation with a fixed displacement using the final displacement values (at the final volumes) taken from the previous stage. A load curve was then applied to control the volume displacements to match the total volume for each subsequent stage as shown in Table 7 (see Appendix 4). The injection period, total time, volume injected and total volume for each fixed displacement load curve point is shown in Table 7.

MATLAB scripts were coded to generate the data that defined the load curves and the fixed displacements for each node for FEBio input file. The initial load curve was a simple exponential curve following $y = 1 - 2^{t6}$ where $t = time$. This curve was later altered through feedback to match the volume of the bladder after each injection of fluid at the relevant time points.

The algorithm for volume time matching is:

1. Run the initial FEM analysis.

2. Check the first FEM load curve volume against the injected volume at the same time.

3. Perform a linear interpolation on the difference between the target volume and the volume for the previous injection time. Perform the same for the load curve values.

4. Use linear interpolation to recalculate the load curve value change.

5. Enter the new load curve value and re-run the FEM analysis.

6. Repeat from step 2 until the volumes are within 0.1% of the target volume.

The step size chosen was $1\ s$ and the time steps chosen was 12700, which is the same total time as the *in vivo* data. The maximum and minimum step size chosen was $10\ s$ to reduce the calculation burden but yield a fine enough sample resolution. Although a larger maximum step size would reduce the calculation time at this stage, it would also produce uneven time intervals in the data, leaving gaps in the stress data that is fed into the H-H model. After code optimisations, this model had a run time of approximately 50 minutes for a full calculation, versus 48 hours for the fluid-structure interaction model.

The stress and pressure data were checked to see that they matched the experimental data. The method for this check was an empirical comparison of the pressure curves. If each subsequent volume and the final volumes match, the geometry matches, and the time steps match, adjusting the material properties until the pressure curve matches gives a reasonable approximation of correct material properties. Figure 13 shows the stress curve for a node taken around the short axis centre of the bladder model at node *c*, shown in Figure 18. This curve matches the expectations of the viscoelastic stress response, which should bear a linear relation with the experimental pressure data.

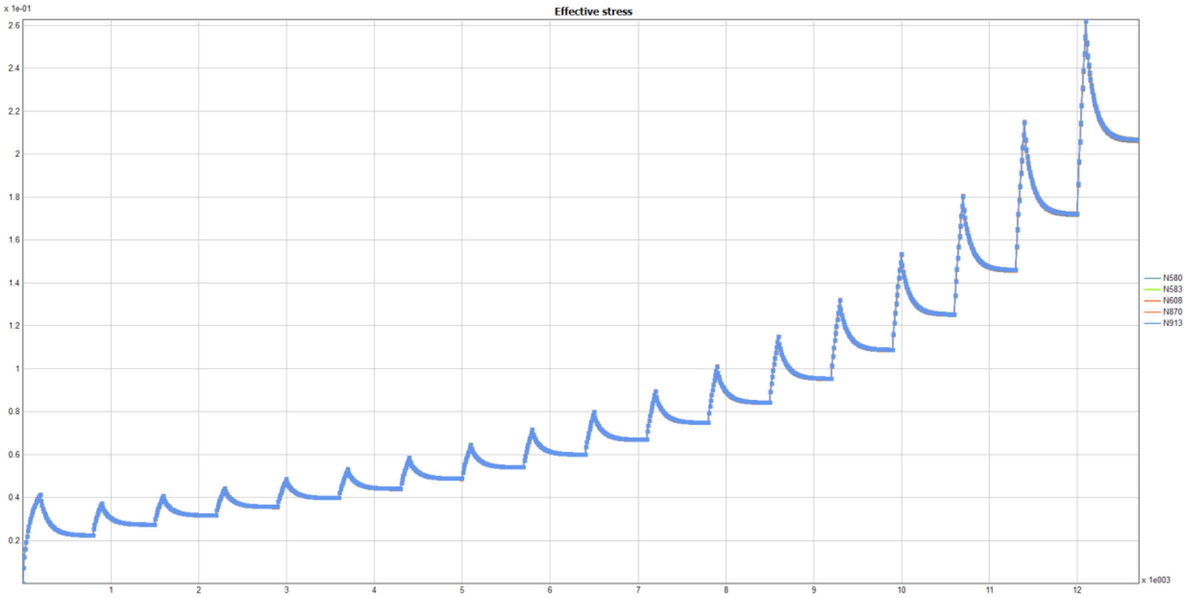

Figure 13 – Stress curve for node c for time t = 0 s to t = 12700 s. Each spike in bladder wall stress is caused by a bladder volume increase. The first volume increase is 100 μL, and each subsequent volume increase is 50 μL.

The pressure was calculated using the stress curve. In PostView, the "effective stress" is selected and output for selected nodes. The effective stress is the Von Mises stresses. PostView cannot calculate the pressure directly on the nodes. Instead the stress curve for node *c* is turned into a pressure curve using a thin wall pressure vessel analysis.

$$inner\ pressure = p = \frac{2t\sigma}{r}$$

Where $p = pressure, t = thickness, \sigma = stress$, and $r = radius$.

The thin wall pressure vessel analysis was formulated for cylindrical vessels. This presents limitations in the accuracy of using thin wall pressure vessel formulation for an prolate spheroid. Other studies have used this approach to calculate pressure in the bladder (Watanabe et al. 1981).

The outer and inner displacement positions are taken and fed into a MATLAB script (see Appendix 3), which converts the stress into pressure at each time step. Figure 14 shows the pressure curve for the node stress curve shown in Figure 13.

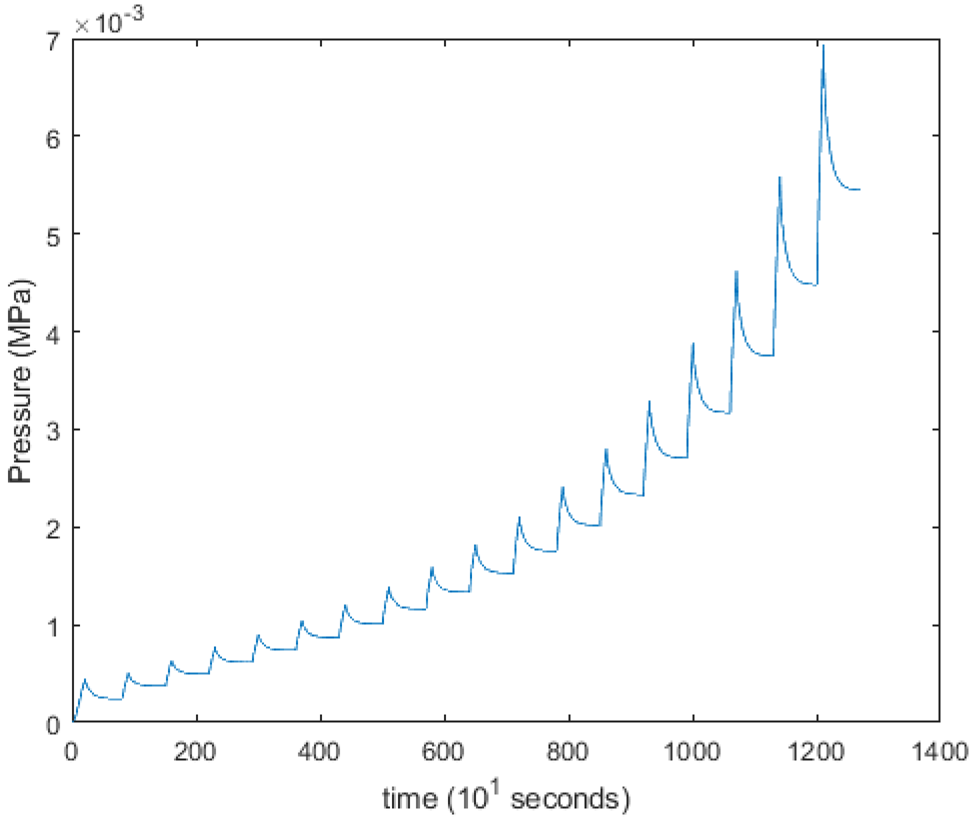

Figure 14 – Calculated pressure curve for node c for time t = 0 s to t = 12700 s. Each spike in bladder wall pressure is caused by a bladder volume increase. The first volume increase is 100 μL, and each subsequent volume increase is 50 μL. Peak pressure at t = 12700 s is 0.0068 MPa = 51 mmHg.

The pressure curve for the Wade model is a close fit to the pressure curve data shown in Figure 6, reaching a peak pressure of 0.0068 MPa = 51 mmHg at t = 12700 s at a volume of 1026 μL, in comparison to the peak pressure of 0.00637 MPa at the same time and volume in Figure 6.

The FEM model stress data is passed to the Hodgkin-Huxley model.

3.8 Using the Hodgkin-Huxley Model to generate neural impulse (action potential) frequency

In this model, the nodes within the FEM mesh are each assumed to represent a mechanoreceptor in the bladder wall. Within Xu's (2007) data in the mechanosensitive pelvic pathway nerves, the muscular and muscular/urothelial receptor fields are shown to be evenly distributed across the bladder and are sensitive to stretch. The nodes in the FEM model will represent a simplified combined model of these nerves. The aim of the Hodgkin-Huxley model is to take the stress output from the FEM model nerves and use it as the input stimulus to the Hodgkin-Huxley model to generate a voltage output. The voltage output models the neural response (action potentials) of the bladder to the stretch of the bladder wall from its volumetric displacement.

A neuron's action potential firing rate is often referred to in the literature as the "impulse rate", i.e. nerve impulses per second. In this research the rate of neuronal action potentials measured per second will be measured and referred to as the firing rate, in Hz.

The firing rate of the action potentials over time can be measured and compared to existing data for mouse neural response to bladder stretch on filling.

Starting with base Hodgkin-Huxley code provided by Professor Mark Taylor (personal communication, April 2019), the code was altered to two sets of code to respectively add both a linear relationship, $I_{mech} = c\sigma_n$, and an exponential relationship, $I_{mech} = c(\mathrm{e}^{\sigma_n})$, where c is a constant, between the current stimulus and the stress values. Constants, variables and functions for modelling the basic action potential were assigned in accordance with Xu et al. (2008) and Shapiro and Lenherr (1972) papers. A function to read in the stress values and store these values to an array was added. The stress value from the FEM model is evaluated every 10 seconds. The Hodgkin-Huxley code evaluates the inputs at a frequency of $20000\ Hz$. The Hodgkin-Huxley code needs a stress value for every $dt = 0.05\ ms$. A function was added to interpolate the stress values with $dt = 0.05\ ms$ intervals between values. The interpolation type chosen was MATLAB's Piecewise Cubic Hermite Interpolating Polynomial (PCHIP), which avoids interpolation curve overshoot.

The Hodgkin-Huxley model generates action potentials for the neural output given an input, in this research it is stress values. A 0.5 second segment of stress input from a single node on the bladder model generates action potentials from the Hodgkin-Huxley model as shown in Figure 15.

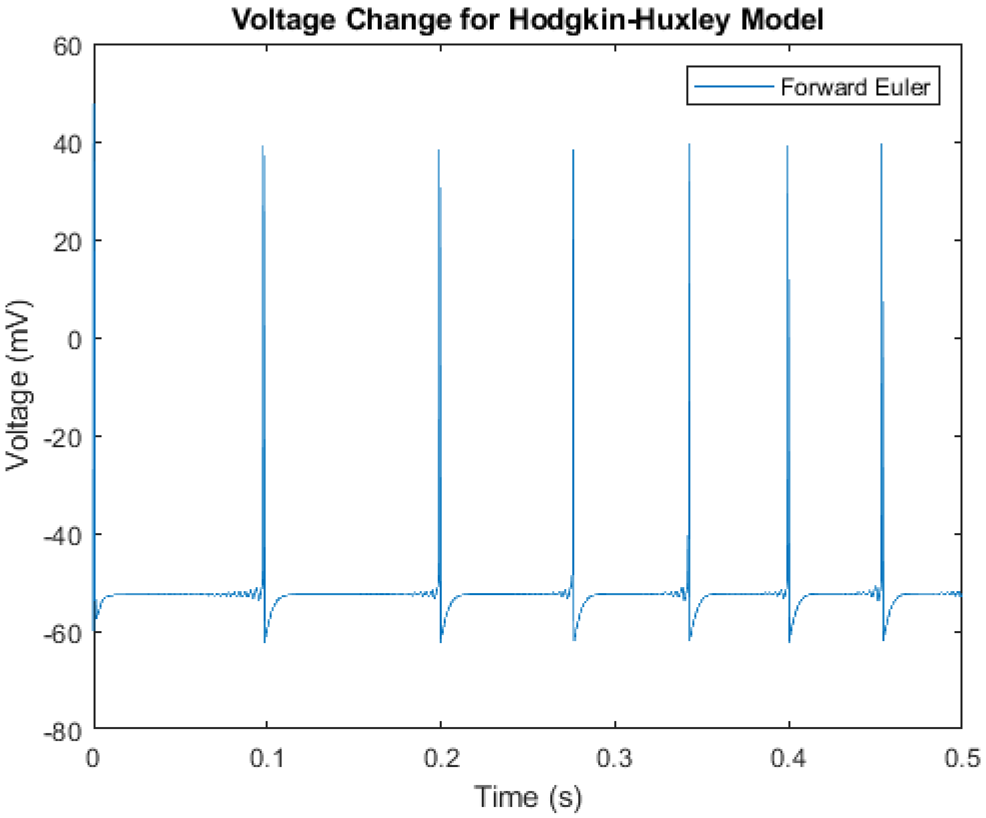

Figure 15 – Action potentials generated by the Hodgkin-Huxley model for node c given a 0.5 s stress input.

The nerves combine signals from multiple points on the bladder from a small receptor field. The stress values feeding into the model replicate several receptors on a receptor field and/or multiple overlapping receptor fields. The research tests for increased node count until a representative output is found. An assumption is made that each receptor does not activate at the same time. The stress values from the FEM model, when taken from node positions that simulate a receptor field, have very little variance.

When the receptors fire in unison, the voltage changes nearly proportionally to how many receptors are chosen, and the firing rate stays the same as for a single node. Figure 16 shows the combined voltage output from a 0.5 second segment of nearly coincident stress input for two nodes.

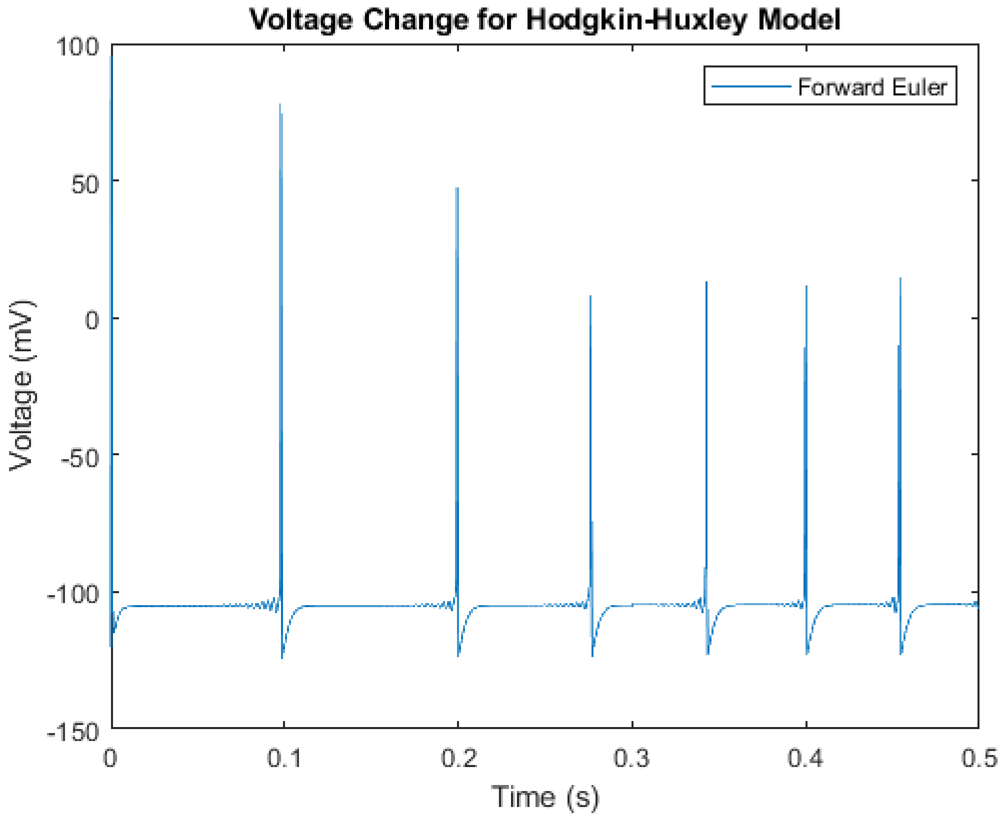

Figure 16 – Combined neural output from two nodes in a small receptor field result in added voltages and no change in firing rate.

Firing in complete unison as shown in Figure 16 above is not supported by data shown in Xu et al. (2008) and Daly et al. (2014), which shows substantial greater variation in firing rate. To simulate different firing times, the stress values from subsequent bladder nodes are forward offset in time. Random time offsets, fixed time offsets as a function of how many nodes were input, and a fixed time offset regardless of how many nodes were input were tried. A fixed time offset was selected for repeatability in the results. When the receptors fire in an offset fashion, the voltages only increase when the waves randomly coincide, which more closely matches the data. Figure 17 shows the same $0.5\ second$ segment of offset stress inputs for two nodes. The time offset is $0.025\ seconds$. Figure 17 shows that the stress values offset in time before being fed into the Hodgkin-Huxley model give an increase in firing rate for the model and no increase in voltage response.

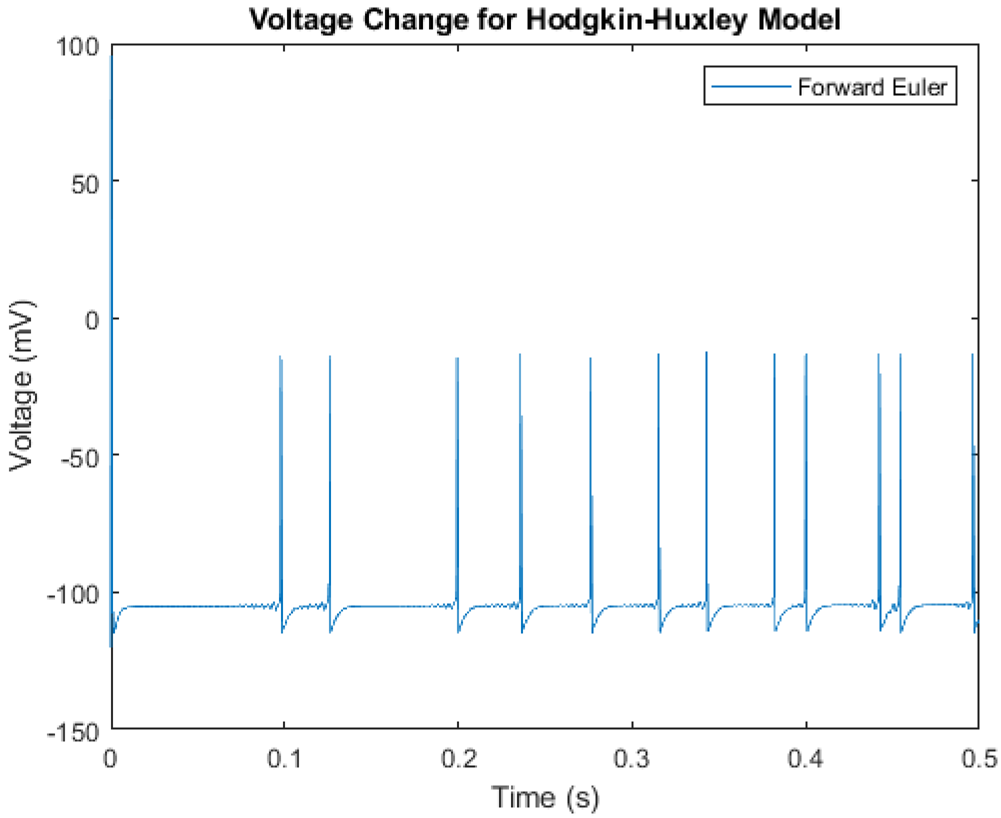

Figure 17 - Two almost identical stress values offset in time result in distinct voltage waveforms and increased firing rate.

The values of k, which is a constant that alters the model's action potential firing rate sensitivity, and γ, which can improve very low frequency firing, were altered during multiple runs of the code to move the firing rate up or down to produce firing rates that matched the *in vitro* data.

The stress value range (minimum to maximum) from the FEM model did not correlate with the input range for I_{st} in the H-H model, and were input as either a linear or exponential function of the FEM model stress output values. The input range of the Hodgkin-Huxley model is scaled between values of $I_{st} = -3.25$ and $I_{st} = 150.0$ which produces firing rates in the range of 0.3 Hz to approximately 50 Hz.

For the total time evaluated, 12700 $seconds$, the Hodgkin-Huxley model code is very memory intensive, utilising > 30 GB of system memory at times in the calculation. To reduce the memory footprint, almost all variables are cleared at the end of calculating the voltages for each node’s code loop. At the end of calculation the final voltages for each node are stored in an array. These voltages are added into a new array with the principal of superposition.

The firing rate for the nodes examined are calculated using MATLAB’s *findpeaks* function. *Findpeaks* finds peaks within the signal within user defined limits. The number of peaks found is divided by the time length examined, in this research for periods of 10 seconds, which gives the firing rate for that time period.

The calculated Hodgkin-Huxley values are displayed as firing rate graphs with results displayed in the results section.

4. Results

This section shows the results obtained and is followed by a discussion of the results. The results from the Hodgkin-Huxley model using data output from the FEM model are shown below with an analysis of each sub-section made in the discussion.

4.1 Node position on a simplified prolate spheroid bladder

Single nodes at different positions were tested for firing rate. Due to the symmetrical nature of the bladder model, data from a 90° segment of the bladder is replicated in all other segments of the bladder, removing the need to analyse more than a 90° arc. The position of the nodes tested are shown in Figure 18.

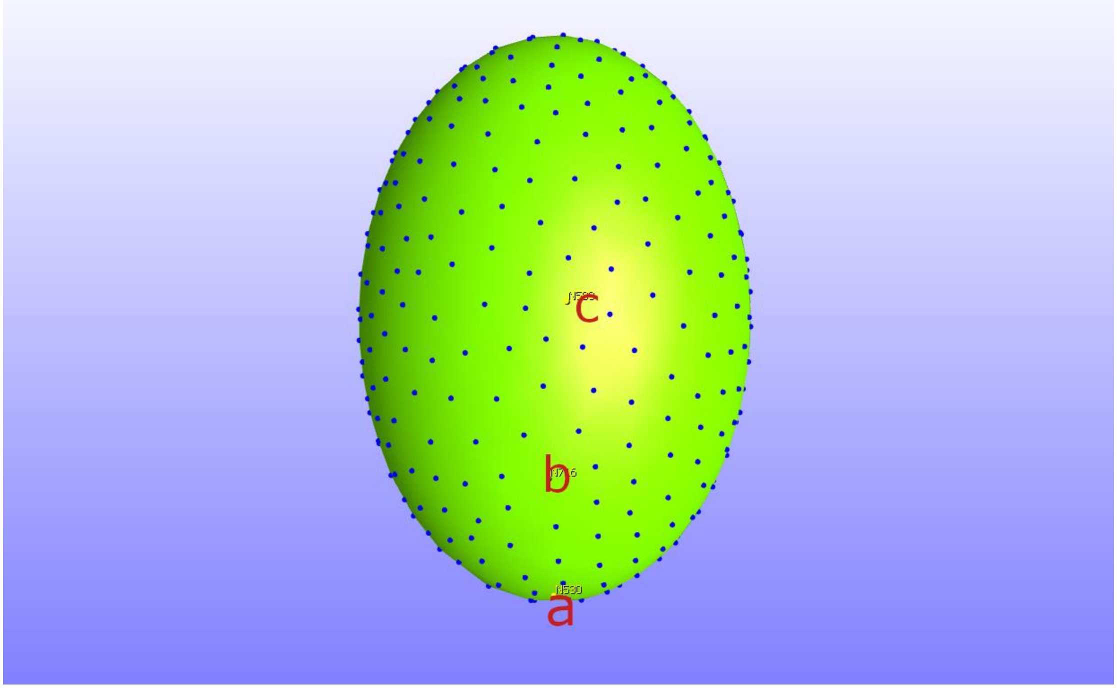

Figure 18 – Positions of node a (at bottom), node b (at 45°), and node c at (90°) on the bladder wall.

The stress output for the three nodes are shown in Figure 19.

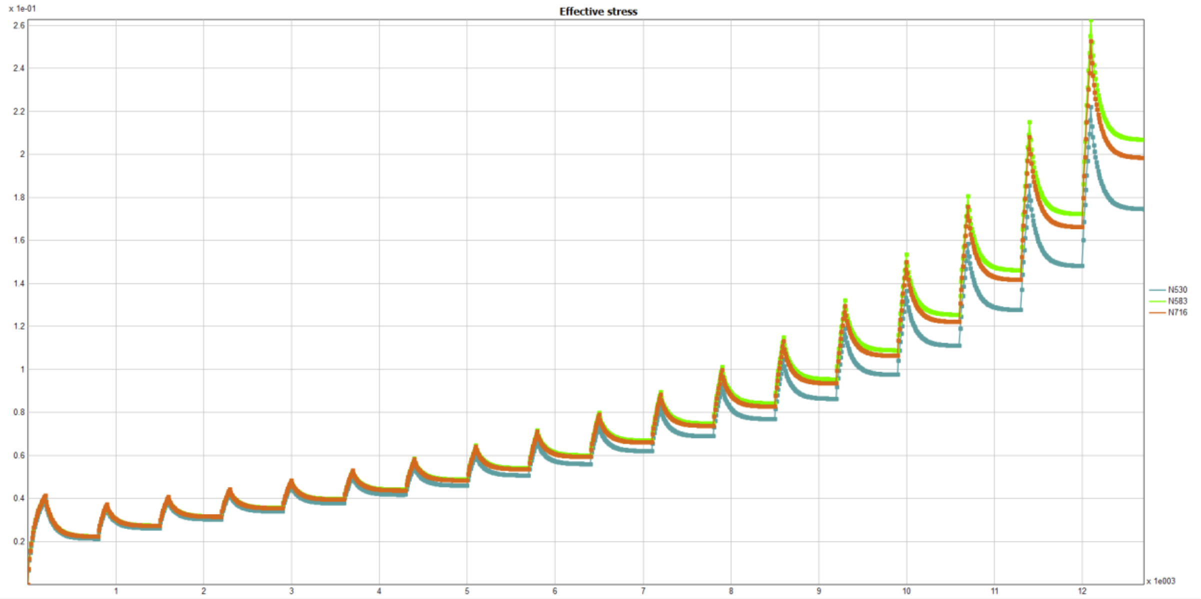

Figure 19 – Stress curves for node a (turquoise), node b (orange), and node c (bright green). This shows the stress measured simultaneously at nodes a, b, and c for t = 0 s to t = 12700 s. Each spike in bladder wall stress is caused by a bladder volume increase. The first volume increase is 100 μL, and each subsequent volume increase is 50 μL. Peak pressure at t = 12700 s is 0.0068 MPa = 51 mmHg.

4.2 Linear Stress Input Function Results

Firing rate results modelled from a linear input function with changes in node position are shown in Figures 20, 21 and 22 for nodes *a*, *b*, and *c,* respectively.

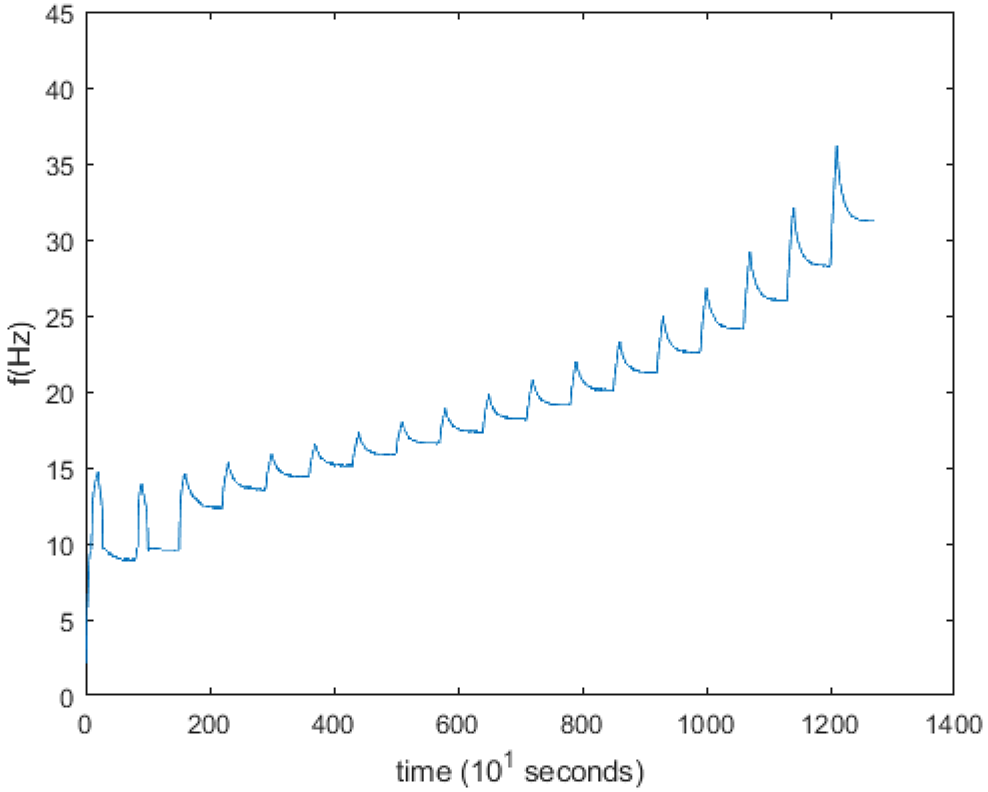

Figure 20 – Firing rate for single node a for t = 0 s to t = 12700 s. The firing rate starts at approximately 10 Hz and peaks at approximately 35 Hz.

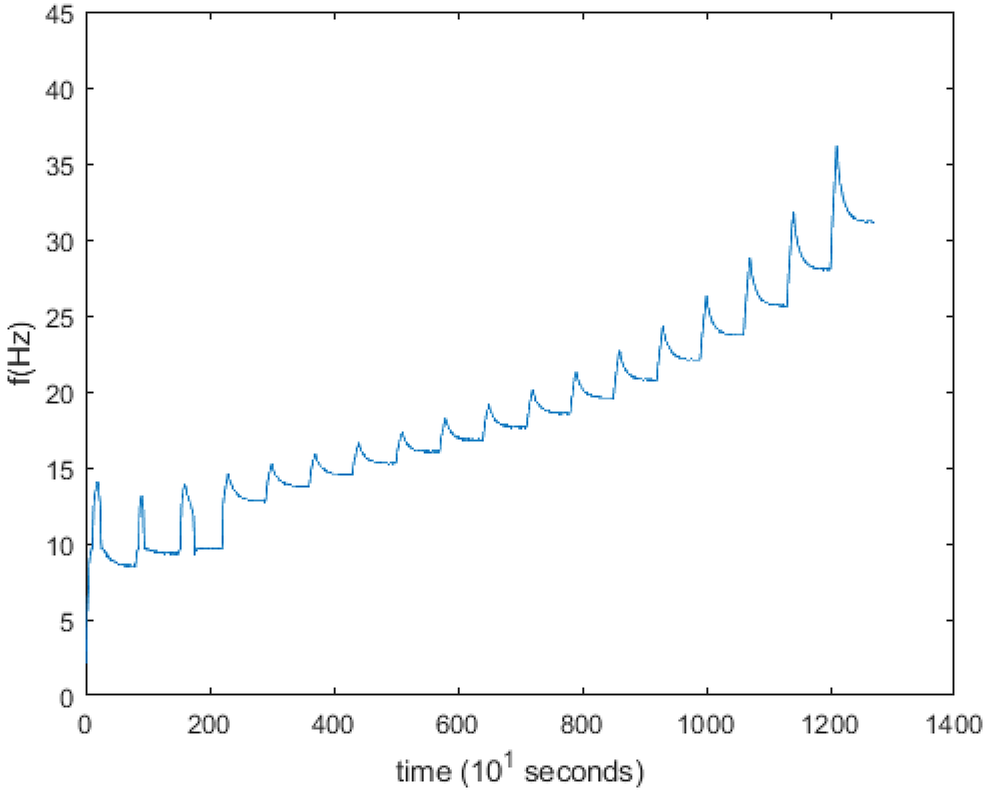

Figure 21 – Firing rate for single node b for t = 0 s to t = 12700 s. The firing rate starts at approximately 10 Hz and peaks at approximately 37 Hz.

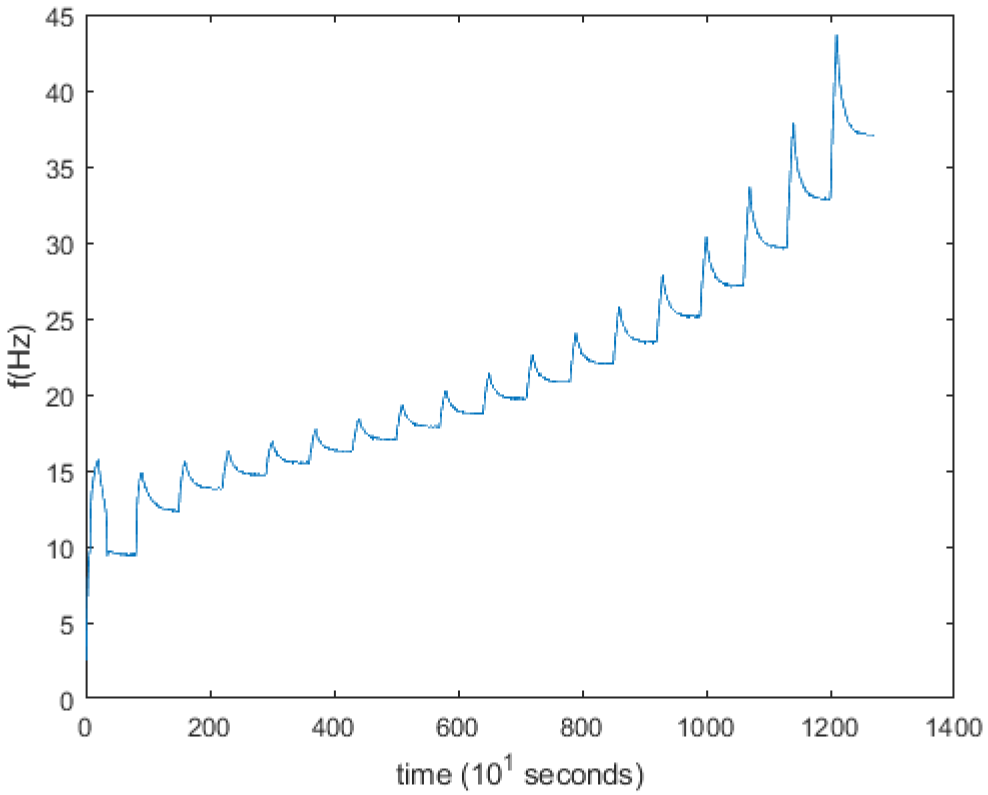

Figure 22 – Firing rate for single node c for t = 0 s to t = 12700 s. The firing rate starts at approximately 10 Hz and peaks at approximately 45 Hz. The peak firing rate changes with the node position.

To simulate a multi-receptor field, groups of three to five nodes in clusters were tested for firing rate in the same position as the previous single node analysis, node cluster positions are shown in Figure 23.

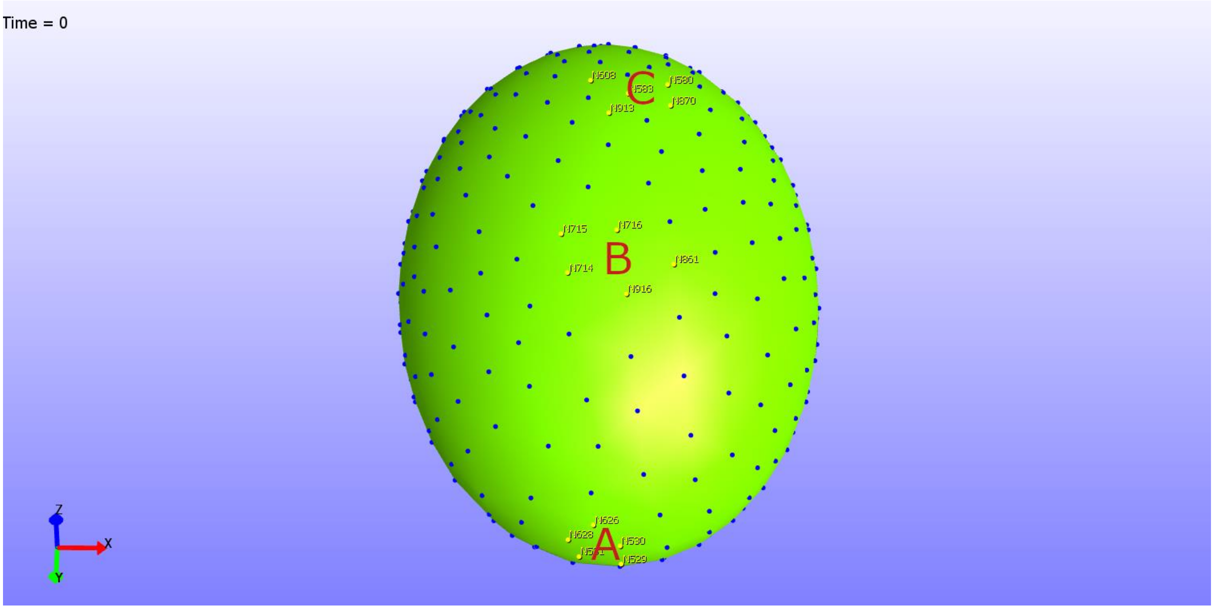

Figure 23 - Positions of node clusters: node cluster A (at bottom), node cluster B (at $45°$), and node cluster C at ($90°$). This bladder is rotated towards the viewer to show the node clusters.

The multi-receptor stress output for the three node clusters are shown in Figure 24.

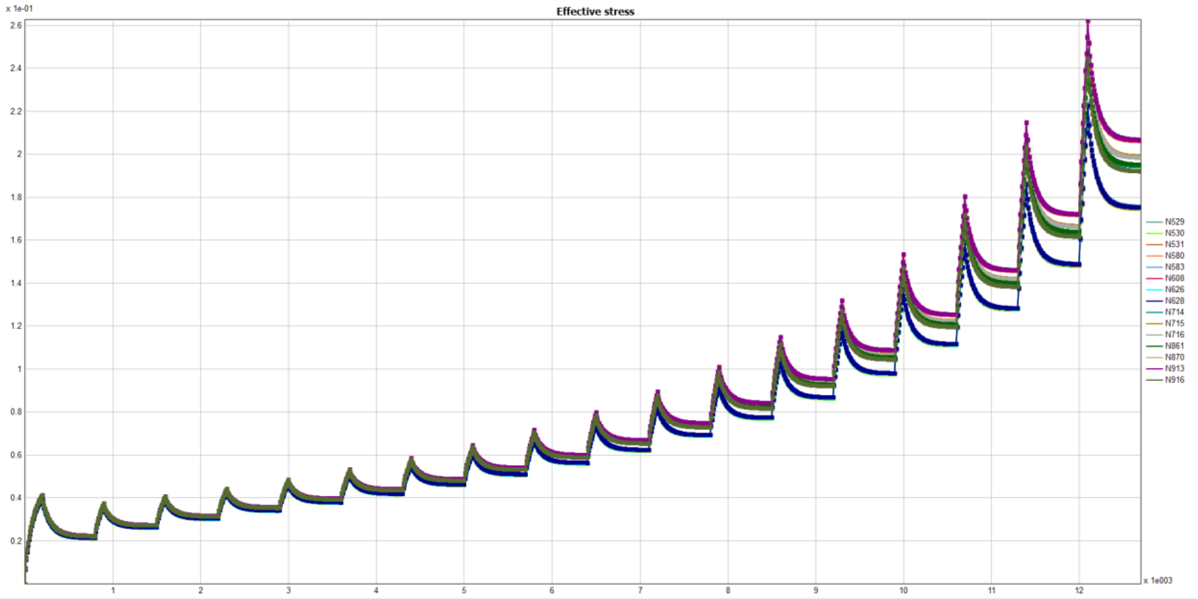

Figure 24 - Stress curves for all nodes in clusters around nodes A, B, and C. This shows the stress measured simultaneously for node clusters A, B, and C for t = 0 s to t = 12700 s. Each spike in bladder wall stress is caused by a bladder volume increase. The first volume increase is 100 μL, and each subsequent volume increase is 50 μL. Peak pressure at t = 12700 s is 0.0068 MPa = 51 mmHg.

Increasing the node count at node cluster C from one node to three, then five nodes, are shown in Figures 22, 25, and 28, respectively.

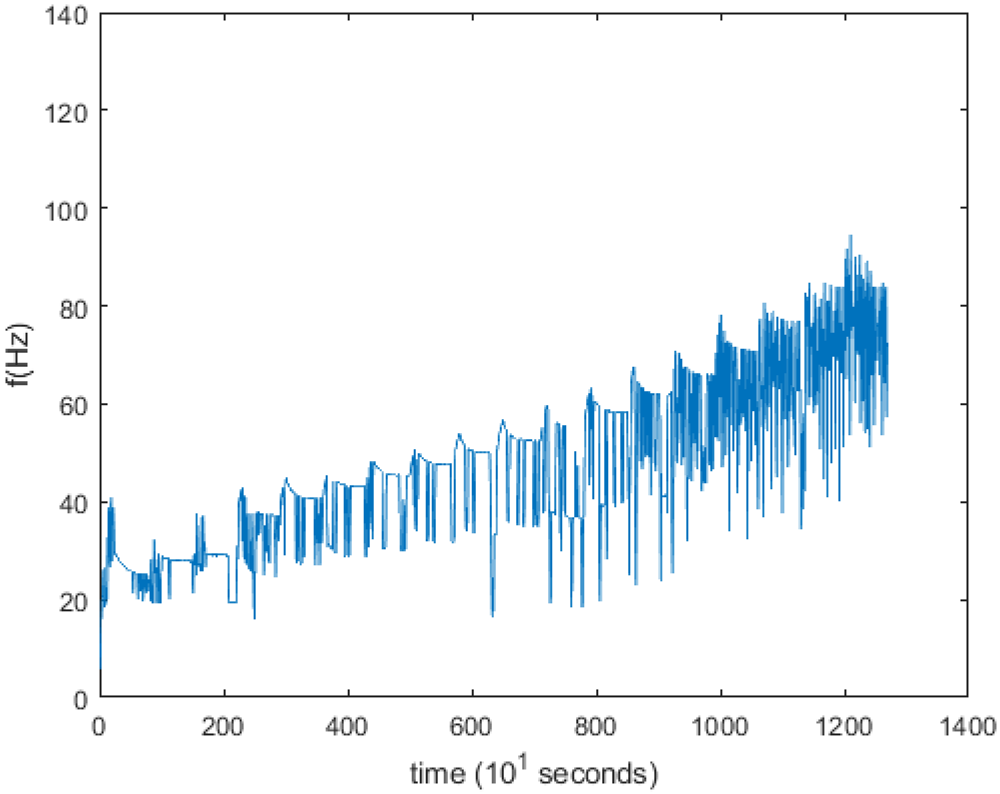

Figure 25 – Firing rate for node cluster C, 3 nodes selected, for t = 0 s to t = 12700 s. The firing rate starts at approximately 20 Hz and peaks at approximately 90 Hz.

Firing rate for the multi-node cluster as a function of position, with five nodes selected in each cluster, are shown in Figures 26, 27 and 28.

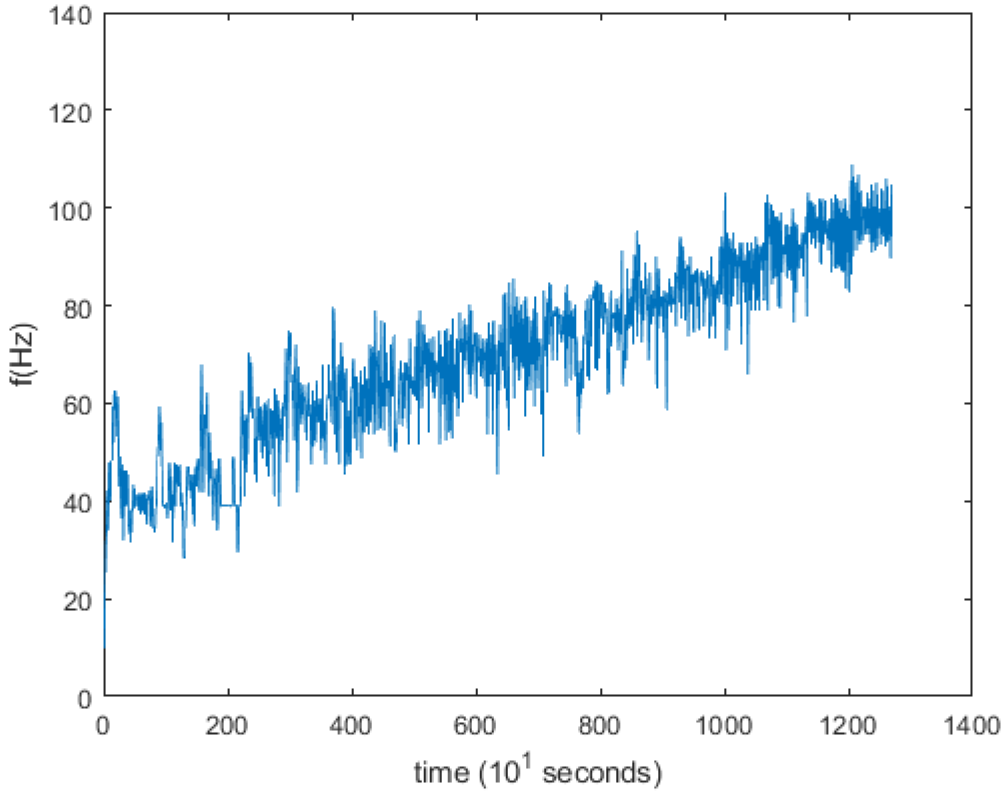

Figure 26 – Firing rate for node cluster A, 5 nodes selected, for t = 0 s to t = 12700 s. The firing rate starts at approximately 40 Hz and peaks at approximately 100 Hz.

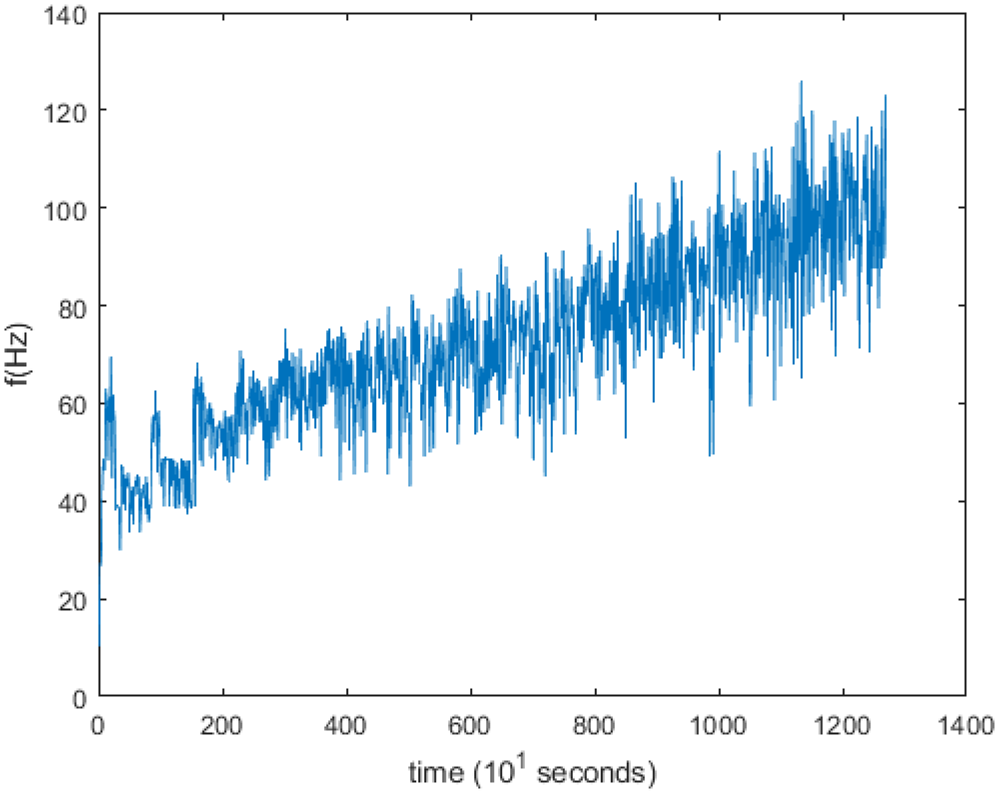

Figure 27 – Firing rate for node cluster B, 5 nodes selected, for t = 0 s to t = 12700 s. The firing rate starts at approximately 40 Hz and peaks at approximately 120 Hz.

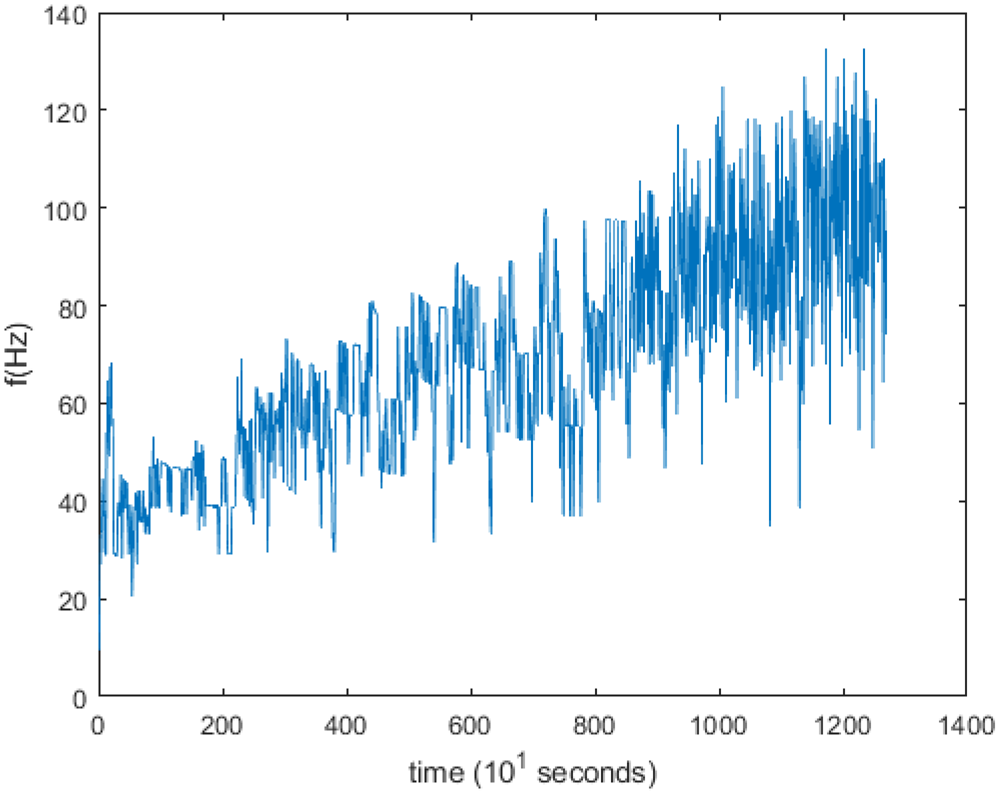

Figure 28 – Firing rate for node cluster C, 5 nodes selected, for t = 0 s to t = 12700 s. The firing rate starts at approximately 40 Hz and peaks at approximately 130 Hz.

The multi node cluster firing rate and stress values for node cluster C are shown in Figure 29.

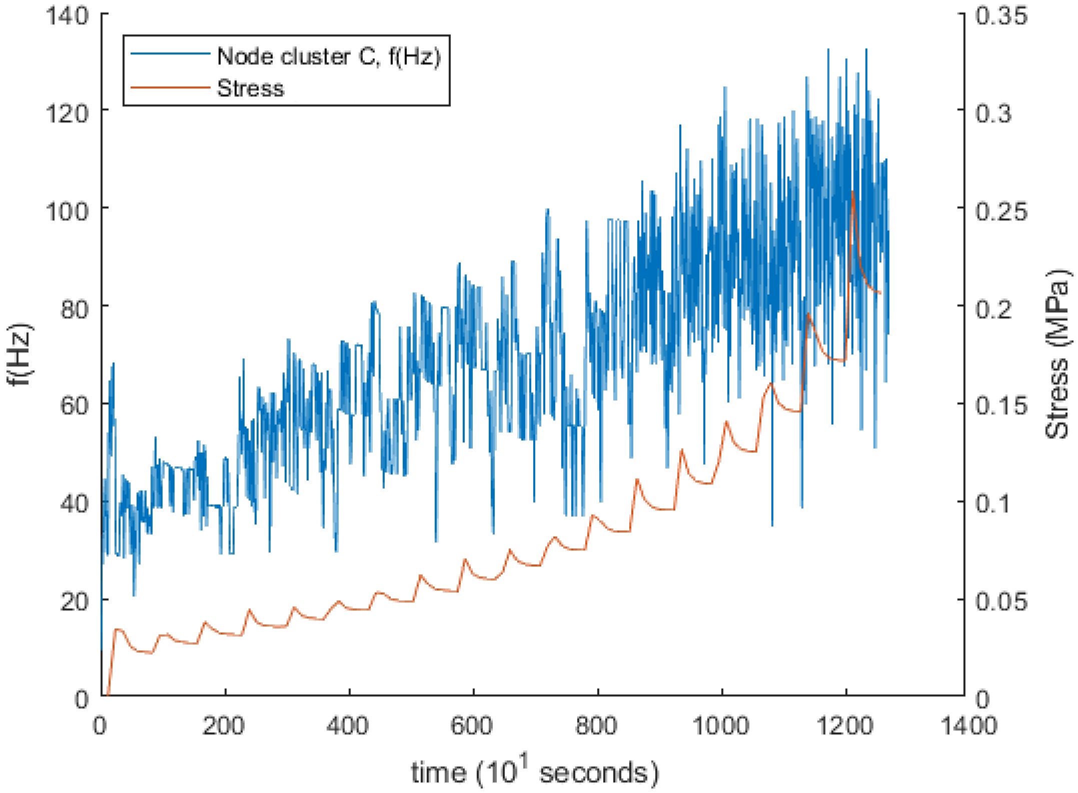

Figure 29 – Stress input and firing rate for node cluster C modelled with a linear input function.

4.3 Exponential Stress Input Function Results

Firing rate results modelled from an exponential input function for single node c are shown in Figure 30.

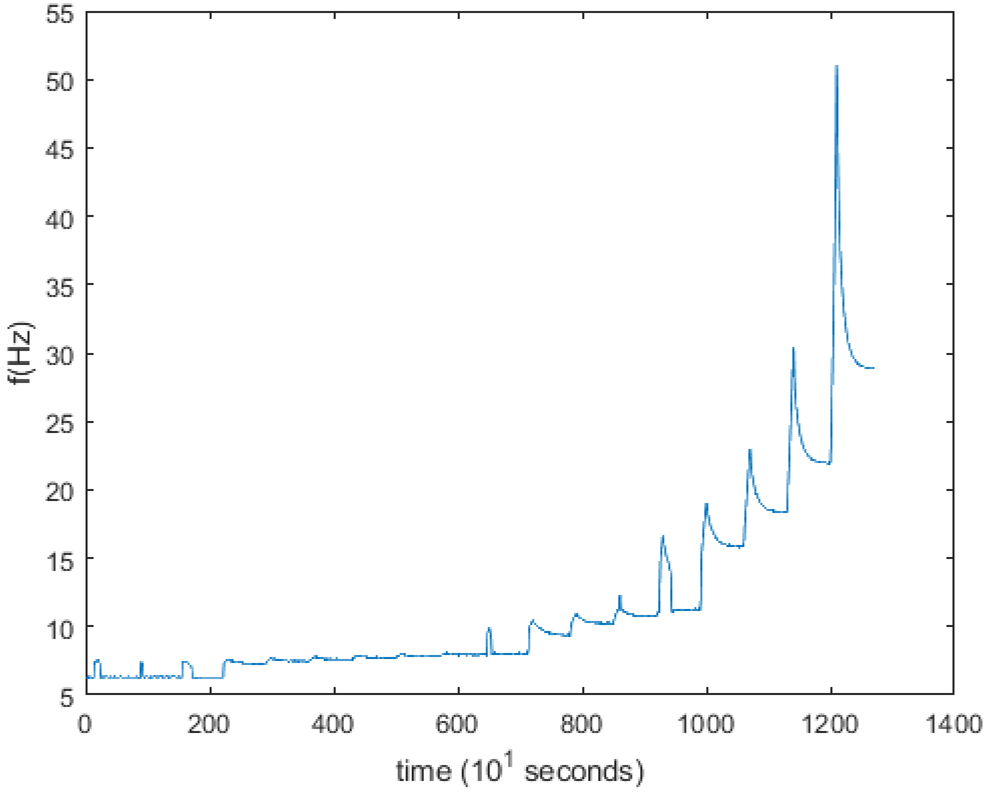

Figure 30 – Firing rate for single node c for t = 0 s to t = 12700 s. The firing rate starts at approximately 7 Hz and peaks at approximately 50 Hz.

The firing rate results modelled from an exponential input function of node cluster C, with 5 nodes selected, are shown in Figure 31.

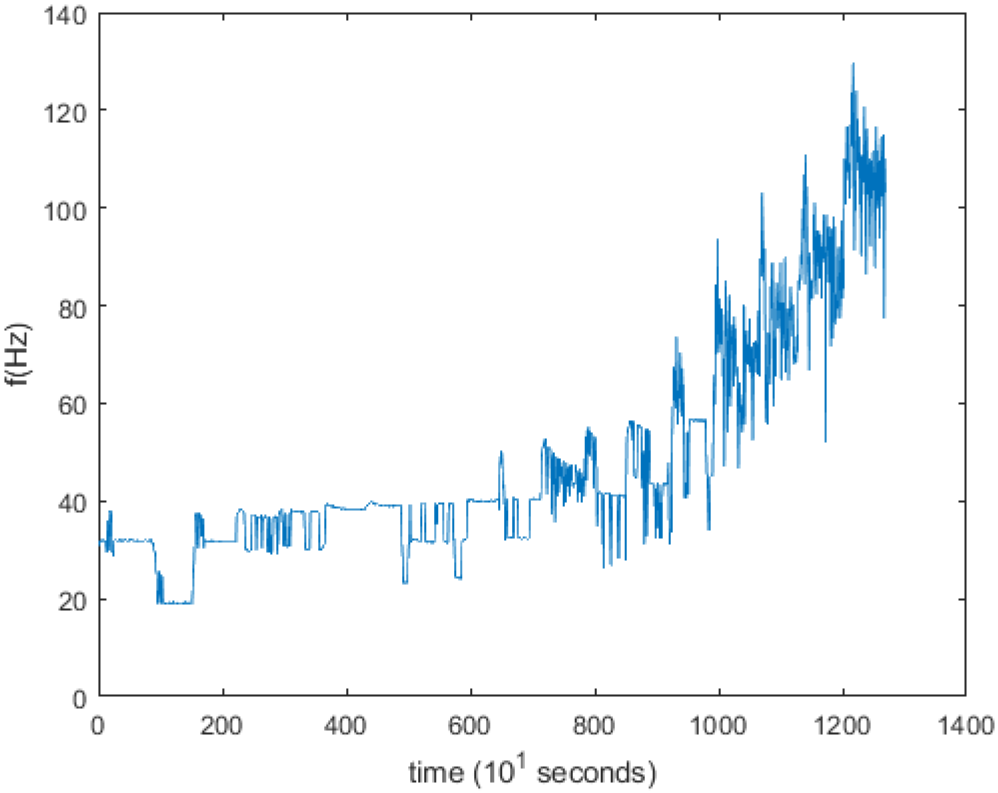

Figure 31 – Firing rate for node cluster C, 5 nodes selected, for t = 0 s to t = 12700 s. The firing rate starts at approximately 35 Hz and peaks at approximately 130 Hz.

The multi node cluster firing rate and stress values for node cluster C are shown in Figure 32.

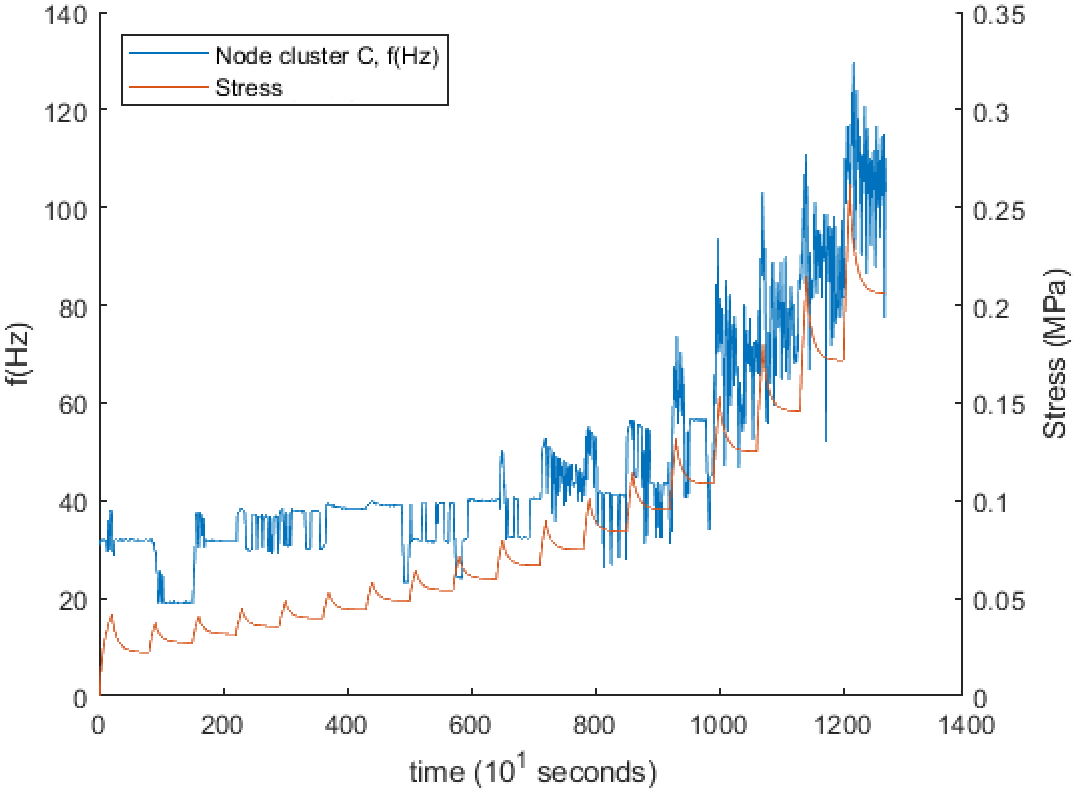

Figure 32 – Stress input and firing rate for node cluster C modelled with an exponential input function.

4.4 Model Validation

A data validation is performed using the data from Daly et al. (2014). The multi-node cluster firing rate modelled as a linear and exponential input are compared to the results from a similar nerve response frequency analysis in Daly et al. (2014), shown in Figures 33, 34 and 35. This model performs a single volumetric inflation over a shorter period of time. Node cluster C, which represents the most compliant part of the bladder and captures the most data, was selected for the analysis.

Image removed due to copyright restriction.

Figure 33 – Firing rate and pressure curve reproduced from Daly (2014).

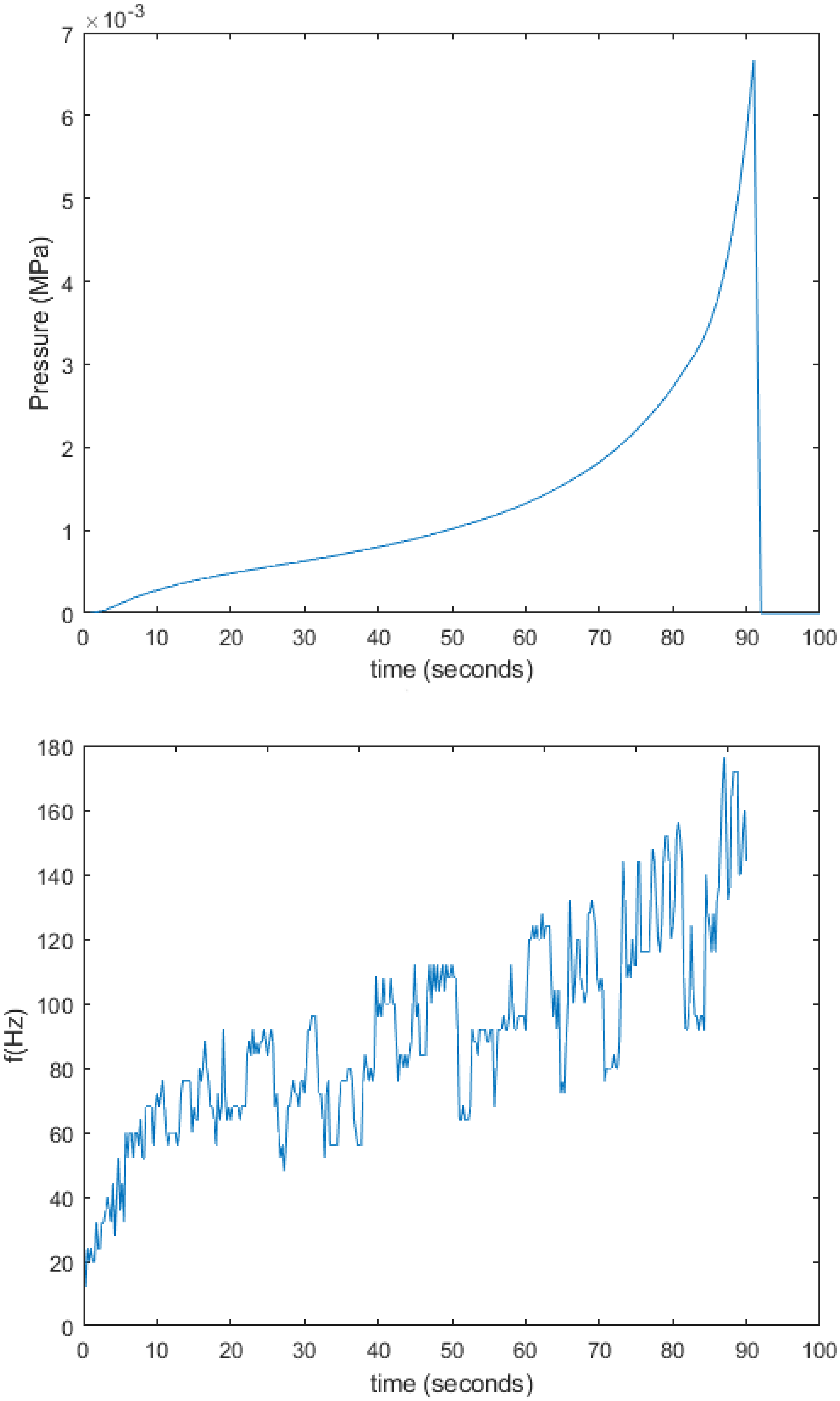

Figure 34 – Multi-node firing rate modelled as a linear input (bottom) and its pressure curve (top). The firing rate starts at approximately 20 Hz and peaks at approximately 180 Hz.

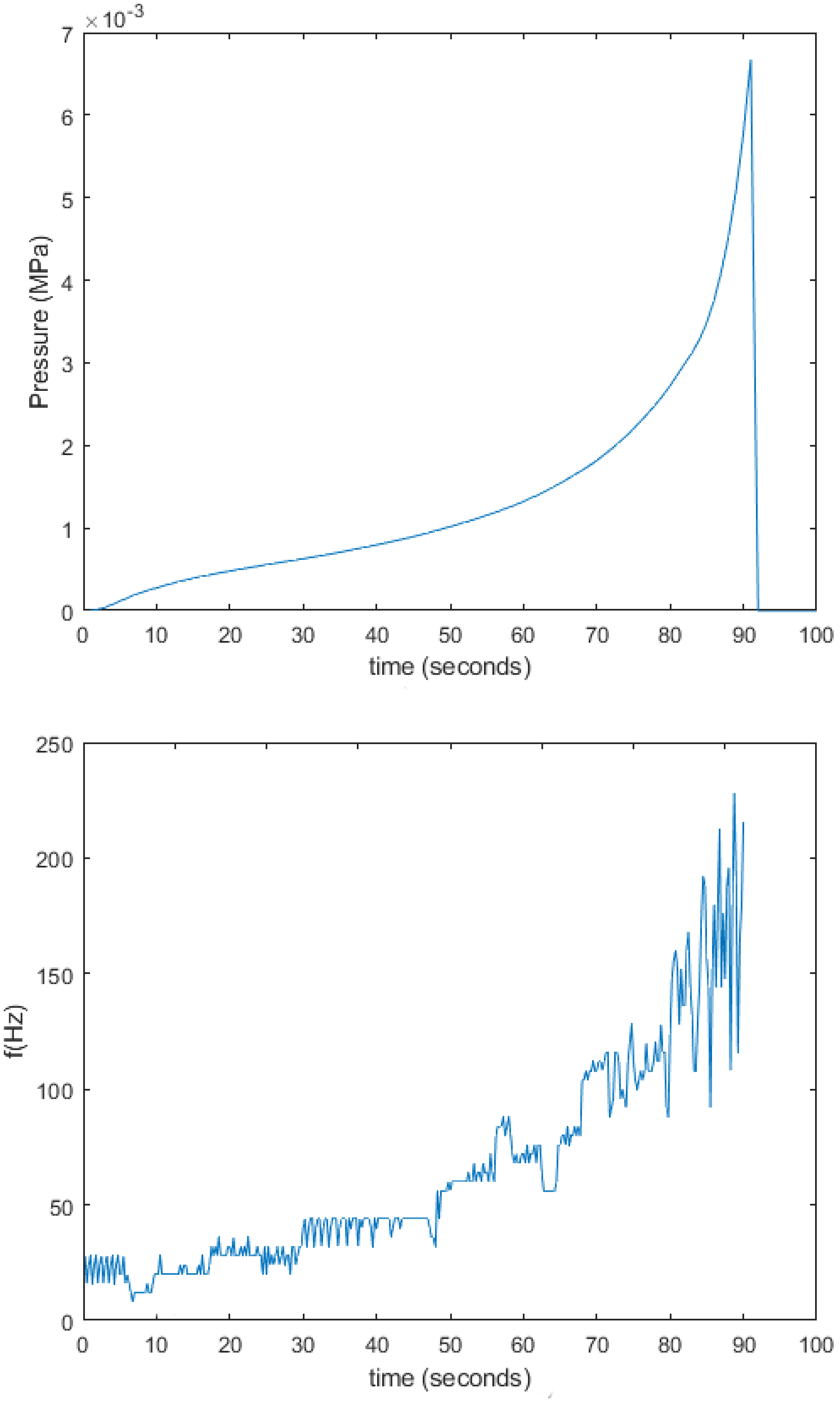

Figure 35 – Multi-node firing rate modelled as an exponential input (bottom) and its pressure curve (top). The firing rate starts at approximately 20 Hz and peaks at approximately 225 Hz.

5. Discussion

5.1 Single node receptor analysis.

The single node results, shown in Figures 20, 21 and 22, for nodes *a* (bottom of model), *b* (offset $45°$), and *c* (offset $90°$), respectively, show the firing rate of each node as a function of both the stress input from the FEM model and the relative position on the model.

When examining the linearly modelled firing rate, node *a* shows a neural output firing rate starting at approximately $10\ Hz$ which increases to approximately $35\ Hz$. The firing rate increases non-linearly with the increase in stress in the bladder wall. Nodes *b* and *c* show a similar increase in firing rate, with a non-linear relationship to the increase in stress in the bladder wall. Nodes *b* and *c* show increasing magnitude of firing rate from the increased stress magnitude for each subsequent node as a function of its position on the bladder, with the upper frequency limit of node *c* increasing to approximately $45\ Hz$.

When examining the exponentially modelled firing rate, node *c* shows a neural output firing rate starting at approximately 7 Hz which increases to approximately $50\ Hz$, increasing non-linearly with the increase in stress in the bladder wall. The exponentially modelled firing rate displayed a larger frequency range than the linearly modelled firing rate.

Each node displays a stress relaxation decrease in firing rate as a function of the viscoelastic behaviour of the bladder.

The geometry of the bladder is seen to affect the firing rate of the nodes, where the smaller radius at the tip of the prolate spheroid bladder presents a stiffer material response, as seen in the lower firing rate of node *a* compared to node *c*.

The prolate spheroid bladder is symmetrical, and it is expected that the firing rate for the top of the bladder will mirror the bottom of the bladder at the same relative node positions.

The results from the single node analyses support the aim of the thesis in modelling firing rate as a function of the stress response output from the FEM model of a bladder. These results represent a single receptor in a receptor field and do not adequately show a response that correlates well with the magnitude of *in vitro* measurements of bladder firing rate from multiple receptors in a receptor field.

5.2 Multi Node Receptor Analysis

The multi node receptor field results, shown in Figures 26, 27, and 28 for node clusters *A* (bottom of model), *B* (offset $45°$), and *C* (offset $90°$) respectively, show the multi-node firing rate of each node as a function of both the linearly modelled stress input from the FEM model and the relative position on the model.

When examining the linearly modelled firing rate, node cluster *A* shows a neural output firing rate starting at approximately 40 Hz which increases to approximately 100 Hz, increasing non-linearly with the increase in stress in the bladder wall. Node cluster *B* and node cluster *C* show the same increase in firing rate, with a non-linear relationship to the increase in stress in the bladder wall.

When examining the exponentially modelled firing rate, node cluster *C* shows a neural output firing rate starting at approximately 35 Hz which increases to approximately 130 Hz, increasing non-linearly with the increase in stress in the bladder wall. The exponentially modelled firing rate displayed a larger frequency range than the linearly modelled firing rate.

The multi node clusters show a change in firing rate as a function of the position and viscoelastic behaviour of the bladder. As the node clusters move towards the most compliant section of the bladder the viscoelastic response can be more readily seen in the waveform. The lower firing rate in less compliant areas of the bladder, such as the lower compliancy around apex of the prolate bladder, which coincides with the position of the trigone area of the bladder (the area that is encompassed by the urethra and two ureters), corresponds with higher nerve density as per Figure 5. The higher nerve density in less compliant areas may be an evolution to maintain firing rate similar to the more compliant areas with lower nerve density.

The geometry of the bladder affects the firing rate of the node clusters, where the smaller radius at the tip of the prolate spheroid bladder presents a stiffer material response.

The prolate spheroid bladder is symmetrical, and it is expected that the multi-node firing rate for the top of the bladder will mirror the bottom of the bladder at the same relative node positions.

The multi-node clusters show a higher firing rate from the bladder wall stress than a single node nerve as can be seen by comparing the single node *c* firing rate in Figure 22 and the node cluster *C* firing rate in the same position in Figure 28.

When the stress input is linear, and firing rate and stress values are plotted against each other, it can be seen there is a non-linear relationship between the stress input and the node cluster firing rate.

When the stress input is non-linear, and the firing rate and stress values are plotted against each other, it can be seen there is a close to linear relationship between the stress input and the firing rate.

The results from the multi node cluster analysis using an exponential function for the stress input support the aim of the thesis in modelling firing rate as a function of the stress response output from the FEM model of a bladder. Moreover, these results model multiple nerve receptors in a receptor field and show a firing rate that correlates with *in vitro* measurements of bladder response from multiple receptors in a receptor field.

5.3 Model Validation

The results from the Daly model show a higher frequency output which corresponds to the much higher stress induced from inflating the bladder to full distention over a much shorter time period, approximately $90\ s$ versus $1900\ s$. The exponentially modelled stress input to the Hodgkin-Huxley model gives an output that closely matches the data in Figure 33. The linearly modelled stress input to the Hodgkin-Huxley model does not give an output that matches the data in Figure 33.

5.4 Significance, limitations, and future work.

This research is significant in several ways. The crux of the research lies in taking an *in vitro* dataset, modelling the properties of the dataset’s original system (i.e. a bladder) as a FEM model, volumetrically inflating the FEM model in line with the *in vitro* volumetric bladder inflation data and using the output from the stress values of this inflation as the stimulus to a modified Hodgkin-Huxley model. The Hodgkin-Huxley model outputs the neural response (action potentials) as a function of the FEM model stress. The firing rates of the action potentials are measured. A successful model of this sort can partially remove the need for future *in vitro* or *in vivo* animal testing for measurements in the same model domain.

This model can alternatively be used to model different biological tissues that have stress and strain in a similar manner and measure their neural output, which in other cases would be analogous to the pain sensation from stretching a tissue, e.g. pain from hyperextension of a joint.

This research has limitations. There was a lack of freely available data on neural output for stretching bladder tissues for mice. The studies available have data in the form of graphs in papers but the primary data sources were not readily available. More bladder pressure volume curve data and neural output data is available for other similar small mammals. The material data for mouse bladder tissue was limited. The geometry data for mouse bladders was limited. The open source nature of the software presented numerous roadblocks. Documentation, software features, and general usability were sometimes greatly lacking. This became most apparent when trying to extend the research to more complex geometries and the difficulties in getting multiple open source software packages to work with each other prevented the completion of this aspect of the research.

The starting code was not designed for very large arrays of input and consequently suffered performance issues. During the research, significant speed and memory requirement improvements were made to the code. The memory footprint was reduced by many gigabytes and the speed was increased by a factor of approximately 2. The original fluid structure interaction dynamic model suffered from severe performance penalties, needing computing resources far beyond what was available.

This work can now be extended with models that present more complex and accurate geometry and focussing on human bladders versus mouse bladders. The much more readily available data on all material properties and geometry (from CT scans and similar) will enhance the accuracy of the model.

6. Conclusion

The action potential firing rate of mouse bladder afferent nerves was modelled using the stress values from a finite element model as a stimulus into a modified Hodgkin-Huxley model. A FEM model replicating *in vivo* mouse bladder dimensions and material properties was constructed and used a two stage finite element analysis to replicate *in vivo* volumetric filling of the bladder. The FEM model was validated against *in vitro* pressure curve data. Stress values from multiple nodes on the finite element model were used as a stimulus into a modified Hodgkin-Huxley model which output the nerves' action potentials as a function of stress. The firing rate of the action potentials was measured. Stress values were input using both a linear relation and an exponential relation. Single nodes were examined showing that firing rate changes as a function of position for models where the stiffness changes as a function of position. A stepped increase in node count stimulus into the Hodgkin-Huxley model was performed showing that combined multiple node inputs simulate a receptor field, with firing rate increasing as node count increases. The FEM into Hodgkin-Huxley model was validated against existing firing rate data for a pressure volume curve. The exponentially modelled input was found to be a better fit for data validation. The FEM into Hodgkin-Huxley model approach successfully output an action potential neural response using stress values from the FEM model input as a stimulus into a modified Hodgkin-Huxley model and is a novel approach within the field.

The model is limited in scope, making several simplifying assumptions that could be addressed in future research. More complex geometry, more accurate material properties, better validation data and a dynamic fluid-structure interaction FEM model are areas that can be addressed.

References

Anderson, A.E., Ellis, B.J. & Weiss, J.A. (2007). Verification, validation and sensitivity studies in computational biomechanics. *Computer Methods in Biomechanics and Biomedical Engineering*, *10*(3), 171-184.

Argungu, M., Bayram, S., Brook, B., Chakrabarti, B., Clayton, R.H., Daly, D.M., Dyson, R.J., Holloway, C., Manhas, V., Naire, S. & Shearer, T. (2015). Modelling afferent nerve responses to bladder filling. *arXiv preprint arXiv:1510.03119*.

Barnes, S.C., Shepherd, D.E.T., Espino, D.M. & Bryan, R.T. (2015). Frequency dependent viscoelastic properties of porcine bladder. *Journal of the Mechanical Behavior of Biomedical Materials*, 42, 168-176.

Cronin, J. (1987). *Mathematical Aspects of Hodgkin-Huxley Neural Theory,* Vol. 7, Cambridge University Press.

Daly, D. M., Nocchi, L., Liaskos, M., McKay, N.G., Chapple, C., & Grundy, D. (2014). Age-related changes in afferent pathways and urothelial function in the male mouse bladder. *Journal of Physiology*, 592(3), 537-549. doi:10.1113/jphysiol.2013.262634

Damaser, M. S. (1999). Whole bladder mechanics during filling. *Scandinavian Journal of Urology and Nephrology*, 33(201), 51-58.

De Pascalis, R., Parnell, W.J., Abrahams, I.D., Shearer, T., Daly, D.M. & Grundy, D. (2018). The inflation of viscoelastic balloons and hollow viscera. *Proceedings of the Royal Society A*, *474*(2218), 20180102.

De Wachter, S., Smith, P., Tannenbaum, C., Van Koeveringe, G., Drake, M., Wyndaele, J.J. & Chapple, C. (2012). How should bladder sensation be measured? ICI-RS 2011. *Neurourology and Urodynamics*, 31(3), 370-374.

Drumm, B.T., Koh, S.D., Andersson, K.E. & Ward, S.M. (2014). Calcium signalling in Cajal-like interstitial cells of the lower urinary tract. *Nature Reviews Urology*, 11(10), 555-564.

El Sayed, R. F., Morsy, M. M., El Mashed, S. M., & Abdel-Azim, M. S. (200). Anatomy of the urethral supporting ligaments defined by dissection, histology and MRI of female cadavers and MRI of healthy nulliparous women. *American Journal of Radiology,* 189, 1145-1157.

Fry, A.W.C. (1999). Visco-elastic properties of isolated detrusor smooth muscle. *Scandinavian Journal of Urology and Nephrology*, 33(201), 12-18.

Hilton, P. & Stanton, S. (1983). Urethal Pressure Measurements by Microtransducer: The results in symptom-free women and in those with genuine stress incontinence. *British Journal of Obstetrics and Gynaecology,* 90, 919-933.

Hodgkin, A.L. & Huxley, A.F. (1952). A quantitative description of membrane current and its application to conduction and excitation in nerve. *The Journal of Physiology*, *117*(4), 500.

Kattan, P. (2008). *MATLAB Guide to Finite Elements: An Interactive Approach*, 2nd Ed. Springer, Berlin, Germany.

Kendroud, S. and Hanna, A. (2019). Physiology, nociceptive pathways. In *StatPearls [Internet]*. StatPearls Publishing. Retrieved from: https://www.statpearls.com/kb/viewarticle/26536

Le Feber, J., van Asselt, E. & van Mastrigt, R. (2004). Afferent bladder nerve activity in the rat: a mechanism for starting and stopping voiding contractions. *Urological Research*, *32*(6), 395-405.

Logan, D. (2012). *A First Course in the Finite Element Method*. Cengage Learning, Connecticut, USA.

Lotz, H.T., Remeijer, P., van Herk, M., Lebesque, J.V., de Bois, J.A., Zijp, L.J. & Moonen, L.M. (2004). A model to predict bladder shapes from changes in bladder and rectal filling. *Medical Physics*, *31*(6), 1415-1423.

Marieb, E.N., Hoehn, K. & Hutchinson, M. (2012). *Human Anatomy and Physiology* 9th ed., Boston: Pearson, 980-982.

Massey, A. & Abrams, P. (1985). Urodynamics of the Lower Urinary Tract. *Clinics in Obstetrics and Gynaecology,* 12(2), 319.

Miftakhov, R.N. & Wingate, D.L. (1996). Electrical activity of the sensory afferent pathway in the enteric nervous system. *Biological Cybernetics*, 75(6), 471-483.

Morrison, J. (1999). The activation of bladder wall afferent nerves. *Experimental Physiology*, 84(1), 131-136.

Nemoto, I., Miyazaki, S., Saito, M. & Utsunomiya, T. (1975). Behavior of solutions of the Hodgkin-Huxley equations and its relation to properties of mechanoreceptors. *Biophysical Journal*, 15(5), 469-479.

Open Stax College (2013, June 19). *Anatomy and Physiology*. Retrieved from http://cnx.org/content/col11496/1.6/

Pawluk, D.T. & Howe, R.D. (1997). A holistic model of human touch. In *Computational Neuroscience*. Springer, Boston, MA, 759-764.

Pepper, D. W. & Heinrich, J. C. (2017). *The Finite Element Method: Basic Concepts and Applications with MATLAB, MAPLE, and COMSOL*, 3rd ed. CRC Press, Florida, USA.

Purves, D., Augustine, G.J., Fitzpatrick, D., Hall, W.C., LaMantia, A.S., Mooney, R.D., Platt, M.L. & White, L. E. (2017). *Neuroscience, 6th ed.* Sunderland, MA: Sinauer Associates.

Reece, J.B., Meyers, N., Urry, L. A., Cain, M. L., Wasserman, S. A., Minorsky, P. V., et al. (2014). *Campbell Biology Tenth edition: Australian and New Zealand version*. Pearson Education.

Reigner, C. H., Kolsky, H., Richardson, P. D., Ghoniem, G. M., & Susset, J. G. (1983). The elastic behavior of the urinary bladder for large deformations. *Journal of Biomechanics,* 16, 915-922.

Reis, L.O., Sopena, J.M.G., Fávaro, W.J., Martin, M.C., Simão, A.F.L., Reis, R.B.D., Andrade, M.F.D., Domenech, J.D. & Cardo, C.C. (2011). Anatomical features of the urethra and urinary bladder catheterization in female mice and rats. An essential translational tool. *Acta Cirurgica Brasileira*, 26, 106-110.

Shapiro, B. I. & Lenherr, F. K. (1972). Hodgkin-Huxley axon: increased modulation and linearity of response to constant current stimulus. *Biophysical Journal*, 12(9), 1145-1158.

Silverthorn, D. U. (2016). *Human Physiology: An Integrated Approach 7th Edition*. Global., London, England: Pearson. Pp636-637

Spirka, T. A. (2010). *Finite Element Modelling of Stress Urinary Incontinence Mechanics*. Doctoral Thesis, Cleveland State University, Ohio, USA.

Takeuchi, E., Yamanobe, T., Pakdaman, K. & Sato, S. (2001). Analysis of models for crustacean stretch receptors. *Biological Cybernetics*, 84(5), 349-363.

Torkkeli, P.H. & French, A.S. (2002). Simulation of different firing patterns in paired spider mechanoreceptor neurons: the role of Na+ channel inactivation. *Journal of Neurophysiology*, 87(3), 1363-1368.

Tozeren, A. (1986). Assessment of fiber strength in a urinary bladder by using experimental pressure volume curves: an analytical method. *Journal of Biomechanical Engineering*, 108(4), 301-305.

UCL Medical Physics and Biomedical Engineering (2015, September 23). *FEBio Tutorial: AAA example* [Video file]. Retrieved from https://www.youtube.com/watch?v=PvX-AD__3ow&feature=emb_title.

Van Mastrigt, R., Coolsaet, B. L. R. A., & van Duyl, W. A. (1978). Passive properties of the urinary bladder in the collection phase. *Medical and Biological Engineering and Computing*, 16, 471-482.

Watanabe, H., Akiyama, K., Saito, T. & Oki, F. (1981). A finite deformation theory of intravesical pressure and mural stress of the urinary bladder. *The Tohoku Journal of Experimental Medicine*, 135(3), 301-307.

Widmaier, E.P., Raff, H. & Strang, K. T. (2016). *Vander's Human Physiology: The Mechanisms of Body Function 14th ed.* McGraw-Hill, 496-497.

Xu, F., Lu, T. J., & Seffen, K. A. (2008). Skin thermal pain modelling—A holistic method. *Journal of Thermal Biology*, 33(4), 223-237.

Xu, L. & Gebhart, G.F. (2008). Characterization of mouse lumbar splanchnic and pelvic nerve urinary bladder mechanosensory afferents. *Journal of Neurophysiology*, 99(1), 244-253.

Zagorodnyuk, V. P., Gibbins, I. L., Costa, M., Brookes, S. J. & Gregory, S. J. (2007). Properties of the major classes of mechanoreceptors in the guinea pig bladder. *The Journal of Physiology*, 585(1), 147-163.

Zagorodnyuk, V. P., Gibbins, I. L., Costa, M., Brookes, S. J. and Gregory, S. J. (2008). Physiology News Magazine. *Age*, 16(73), p.19.

Zeng, J., Xie, K., Jiang, C., Mo, J. & Lindström, S. (2012). Bladder mechanoreceptor changes after artificial bladder outlet obstruction in the anesthetized rat. *Neurourology and Urodynamics*, 31(1), 178-184.

Appendix 1

```
%%%%%%%%%%%%%%%%%%%%%%%%%%%%%%%%%%%%%%%%%%%%%%%%%%%%%%%%%%%%%%%%%%%%%%%%%%%
%%%%%%%%%%%%%%%%
%
% Harley Ewing 9704959
% Hodgkin-Huxley linear input model to calculate firing rate of action
potentials
%
%%%%%%%%%%%%%%%%%%%%%%%%%%%%%%%%%%%%%%%%%%%%%%%%%%%%%%%%%%%%%%%%%%%%%%%%%%%
%%%%%%%%%%%%%%%%

clear all;
clc;
close all;
format long;
profile on; % Initialise profiler to indentify where code execution is
slowest

%First step - Replicate the work of Xu et al on nociception of skin

filename = 'bladder_18_N583_cluster_stress.txt';
opts = detectImportOptions(filename);
preview(filename, opts);
t1 = readtable(filename, opts);
stress = table2array(t1(:,:));
sz = size(stress); %Find size of array reported as "rows, columns".
C = 5; % How many stress columns
stress(:,1) = stress(:,1)*1000;

stress_node = zeros(254000000,C);
for j_loop = 1:C
    x_int = stress(:,1);
    v_int = stress(:,j_loop+1);
    xq = 0.05:0.05:12700000;
    stress_node(:,j_loop) = interp1(x_int,v_int,xq,'pchip');
end

stress_node_shifted = zeros(254000000,C-1);
shift = 2000; % fixed offset initialisation

if C >= 2
    for i_node = 2:C
        stress_node_shifted((shift+1):end,i_node-1) = stress_node(1:(end-
shift),i_node);
        stress_node(:,i_node) = stress_node_shifted(:,i_node-1);
        shift = shift + 2000; % fixed offset initialisation
    end
end

M = max(stress_node, [], 'all');

dt=0.05; % Time Step ms
t=0:dt:12700000; %Time Array ms
% t=0:dt:5000000; %Time Array ms
t_on_dt = t(1,end)/dt;

V_f = zeros(C, t_on_dt+1);
```

```
for I_ST_loop = 1:C

% Constants and definitions

% Hogdkin Huxley constants
% Original Constants set for all Methods

Cnst_Cm= 1; % Membrane Capcitance uF/cm^2 Cm=0.01

VA = -50;
Cnst_ENa=55; % mv Na reversal potential
Cnst_EK=-72; % mv K reversal potential
Cnst_El=10; % mv Leakage reversal potential
Cnst_gbarNa=120; % mS/cm^2 Na conductance gbar Na=1.2
Cnst_gbarK=36; % mS/cm^2 K conductance gbar
Cnst_gbarl=0.3; % mS/cm^2 Leakage conductance gbarl
epsilon = 1.0;% from Shapiro and Lenherr 1972 epsilon varies between 1 and
10

V(1)= -60; % Initial Membrane voltage
REF_I=0.00; %External Current Applied

% parameters as per squid axon, taken from (Connor et al., 1977;Hille,
1992), Xu p227
GL = 0.3;
A_fac = 7;
B_fac = 7;
Cnst_gbarA = 47.7;
m_fac = 0.263;
h_fac = 0.263;
n_fac = 2.63;

% Declare variable arrays to save time
alpha_A = zeros(1,t_on_dt);
alpha_B = zeros(1,t_on_dt);
alpha_h = zeros(1,t_on_dt);
alpha_m = zeros(1,t_on_dt);
alpha_n = zeros(1,t_on_dt);

beta_A = zeros(1,t_on_dt);
beta_B = zeros(1,t_on_dt);
beta_h = zeros(1,t_on_dt);
beta_m = zeros(1,t_on_dt);
beta_n = zeros(1,t_on_dt);

A = zeros(1,t_on_dt+1);
B = zeros(1,t_on_dt+1);
h = zeros(1,t_on_dt+1);
m = zeros(1,t_on_dt+1);
n = zeros(1,t_on_dt+1);

%Variables
%===set the initial states===%
%V=-0; %Baseline voltage
alpha_n(1) = (1/n_fac) * (epsilon*(-.01 * ( (50+V) / (exp(-(V+50)/10)-1)
))); %Equation 12
beta_n(1) = (1/n_fac) * (epsilon*(.125*exp((-(V+60)/80)))); %Equation 13
```

```
alpha_m(1) = (1/m_fac) * (-0.1*( (V+35) / (exp(-(V+35)/10)-1))); %Equation
20
beta_m(1) = (1/m_fac) * (4*exp(-(V+60)/18)); %Equation 21
alpha_h(1) = (1/h_fac) * (0.07*exp(-(V+60)/20)); %Equation 23
beta_h(1) = (1/h_fac) * (1/(exp(-(V+30)/10)+1)); %Equation 24

%------------for Ik2------------------------------- Currents for 2nd
potassium channel, Xu p227
A_inf = ((0.0761*exp((V+94.22)/31.84))/(1+exp((V+1.17)/28.93)))^(1/3);
Ta_A = A_fac*(0.3632+(1.158/(1+exp((V+55.96)/20.12))));
alpha_A(1) = A_inf/Ta_A;
beta_A(1) = (1-A_inf)/Ta_A;

B_inf = (1/(1+exp((V+53.3)/14.54)))^4;
Ta_B = B_fac*(1.24+(2.678/(1+exp((V+50)/16.027))));
alpha_B(1) = B_inf/Ta_B;
beta_B(1) = (1-B_inf)/Ta_B;



A(1) = alpha_A/(alpha_A+beta_A);
B(1) = alpha_B/(alpha_B+beta_B);
%----------------------------------------------

n(1) = alpha_n/(alpha_n+beta_n); %Equation 9
m(1) = alpha_m/(alpha_m+beta_m); %Equation 18
h(1) = alpha_h/(alpha_h+beta_h); %Equation 18



%Temperature related inputs for the Xu paper
Temp_noci = 55; % nociceptor temperature
Temp_thres = 43; % thermal pain threshold temperature
I_shift = -4; % -4 fudge factor introduced Xu to stop firing below
threshold value This influences the threshold of firing

Ch1 = 0.382; % constant for I_ST, frequency is proportional to this value
Ch2 = 0.064; % constant for I_ST, frequency is inversely proportional to
this value
Ch3 = 0.355;

Tn=[];
f =[];
f2=[];
f3=[];

k_temp = 3^((Temp_noci-6.3)/10);
k = 0.15; %This influences the rate of firing Range 0.03 to 0.15 is
reasonable

% I_ST = (Ch1*exp(((Temp_noci-Temp_thres)/Temp_thres)/Ch2)+Ch3)+ I_shift;
%Xu p231, I_st = stimulation current, eq 36
% as per Xu, I_ST = I_heat + I_chem + I_mech, where chem and mech are
assumed linear variables, p234

I_ST = zeros(t_on_dt,1);
time = zeros(1,t_on_dt);

    for i=1:t_on_dt % = t/dt = total amount of time steps
```

```
        I_ST = stress_node(i,I_ST_loop) * (83.25/M) - 3.25; % node constant
multiplier

        time(i) = i;
        alpha_n(i) =  (1/n_fac) * (epsilon*(-.01 * ( (50+V(i)) / (exp(-
(V(i)+50)/10)-1) )));
        beta_n(i) = (1/n_fac) * ( epsilon*(.125*exp((-(V(i)+60)/80))));
        alpha_m(i) = (1/m_fac) * (-0.1*( (V(i)+35) / (exp(-(V(i)+35)/10)-1)
));
        beta_m(i) = (1/m_fac) * (4*exp(-(V(i)+60)/18));
        alpha_h(i) = (1/h_fac) * (0.07*exp(-(V(i)+60)/20));
        beta_h(i) = (1/h_fac) * (1/(exp(-(V(i)+30)/10)+1));

        %------------------------------for Ik2-------------------
        A_inf =
((0.0761*exp((V(i)+94.22)/31.84))/(1+exp((V(i)+1.17)/28.93)))^(1/3);
        Ta_A = A_fac*(0.3632+(1.158/(1+exp((V(i)+55.96)/20.12))));
        alpha_A(i) = A_inf/Ta_A;
        beta_A(i) = (1-A_inf)/Ta_A;

        B_inf = (1/(1+exp((V(i)+53.3)/14.54)))^4;
        Ta_B = B_fac*(1.24+(2.678/(1+exp((V(i)+50)/16.027))));
        alpha_B(i) = B_inf/Ta_B;
        beta_B(i) = (1-B_inf)/Ta_B;
        %------------------------------------------------------



        %---calculate the currents---%
        I_Na = (m(i)^3) * Cnst_gbarNa * h(i) * (V(i)-Cnst_ENa); %Equations
3 and 14
        I_K = (n(i)^4) * Cnst_gbarK * (V(i)-Cnst_EK); %Equations 4 and 6
        I_L = Cnst_gbarl *(V(i)-Cnst_El); %Equation 5
        I_k2 = Cnst_gbarA * (A(i)^3)* B(i) * (V(i) - VA); % not sure about
VA
        I_ion = I_ST - I_K - I_Na - I_L - I_k2;


        %---calculate the derivatives using Euler first order
approximation---%
        V(i+1) = V(i) + dt*I_ion/Cnst_Cm;
        n(i+1) = n(i) + dt*((alpha_n(i) *(1-n(i)) - beta_n(i) * n(i))*k);
%Equation 7
        m(i+1) = m(i) + dt*((alpha_m(i) *(1-m(i)) - beta_m(i) * m(i))*k);
%Equation 15
        h(i+1) = h(i) + dt*((alpha_h(i) *(1-h(i)) - beta_h(i) * h(i))*k);
%Equation 16



        A(i+1) = A(i) + dt*(alpha_A(i) *(1-A(i)) - beta_A(i) * A(i)); %for
Ik2
        B(i+1) = B(i) + dt*(alpha_B(i) *(1-B(i)) - beta_B(i) * B(i)); %for
Ik2
    end

    V_f(I_ST_loop,:) = V(1,:);
    f3 = f2;

    clearvars -except V_f f3 t dt t_on_dt M stress_node C
end
```

```
% V_f_added = (V_f(1,:) + V_f(2,:)); % Choose this for 2 nodes, etc.
% V_f_added = (V_f(1,:) + V_f(2,:) + V_f(3,:));
V_f_added = (V_f(1,:) + V_f(2,:) + V_f(3,:) + V_f(4,:) + V_f(5,:));
% V_f_added = (V_f(1,:) + V_f(2,:) + V_f(3,:) + V_f(4,:) + V_f(5,:) +
V_f(6,:) + V_f(7,:));

for i = 200000:200000:t_on_dt   %multi node voltage
    temp_peaks = findpeaks(V_f_added(1,i-199999:i),'MinPeakProminence',20);
    freq = (numel(temp_peaks)-1)/(10.0);
    f3 = [f3, freq];
end

% for i = 200000:200000:t_on_dt   %single node voltage
%     temp_peaks = findpeaks(V_f(1,i-199999:i),'MinPeakProminence',20);
%     freq = (numel(temp_peaks)-1)/(10.0);
%     f3 = [f3, freq];
% end

x_axis = 1: t(1,end)/10000;

x1 = 12:12:1270;     %rms calcs
index = 12;
for i = 1:105
   y1(1,i) = rms(f3(1,index-11:index));
   index = index+12;
end

sample_index = 1;    %stress calcs
for i=1:105
stress_sample(1,i) = stress_node(sample_index,1);
sample_index = sample_index + 2419000;
end
stress_sample = stress_sample*400; %stress multiplier for display only

%%
% Plot the functions
figure;
hold on
a1 = plot(x_axis, f3); M1 = 'Node cluster C, f(Hz)';
a2 = plot(x1, stress_sample); M3 = 'Stress (400x)';
% ylim([0 140])
xlabel('time (10^1 seconds)');
ylabel('f(Hz)');
legend([a1;a2], M1, M3, 'Location','northwest')
hold off

figure;
plot(x_axis, f3);
ylim([0 45])
xlabel('time (10^1 seconds)');
ylabel('f(Hz)');

% figure(2)
% plot(t,V_f(1,:));
% legend('Forward Euler');
% xlabel('Time (seconds)');
% ylabel('Voltage (mV)');
% title('Voltage Change for Hodgkin-Huxley Model');
```

```
figure(2)
plot(t,V_f_added(1,:));
legend('Forward Euler');
xlabel('Time (ms)');
ylabel('Voltage (mV)');
title('Voltage Change for Hodgkin-Huxley Model');

profile off; % Terminate profiler
profile viewer; % Display profiler data to indentify where code execution
is slowest
```

Appendix 2

```
%%%%%%%%%%%%%%%%%%%%%%%%%%%%%%%%%%%%%%%%%%%%%%%%%%%%%%%%%%%%%%%%%%%%%%%%%%%
%%%%%%%%%%%%%%%%
%
% Harley Ewing 9704959
% Hodgkin-Huxley exponential input model to calculate firing rate of action
potentials
%
%%%%%%%%%%%%%%%%%%%%%%%%%%%%%%%%%%%%%%%%%%%%%%%%%%%%%%%%%%%%%%%%%%%%%%%%%%%
%%%%%%%%%%%%%%%%

clear all;
clc;
close all;
format long;
profile on; % Initialise profiler to indentify where code execution is
slowest

%First step - Replicate the work of Xu et al on nociception of skin

filename = 'bladder_18_N583_cluster_stress.txt';
opts = detectImportOptions(filename);
preview(filename, opts);
t1 = readtable(filename, opts);
stress = table2array(t1(:,:));
sz = size(stress); %Find size of array reported as "rows, columns".
C = 5; % How many stress columns
stress(:,1) = stress(:,1)*1000;

stress_node = zeros(254000000,C);
for j_loop = 1:C
    x_int = stress(:,1);
    v_int = stress(:,j_loop+1);
    xq = 0.05:0.05:12700000;
    stress_node(:,j_loop) = interp1(x_int,v_int,xq,'pchip');
end

stress_node_shifted = zeros(254000000,C-1);
shift = 2000; % fixed offset initialisation

stress_node(:,:) = exp(stress_node(:,:)*8.25); % exponential transform and
constant multiplier
if C >= 2
    for i_node = 2:C
        stress_node_shifted((shift+1):end,i_node-1) = stress_node(1:(end-
shift),i_node);
        stress_node(:,i_node) = stress_node_shifted(:,i_node-1);
        shift = shift + 2000; % fixed offset
    end
end

M = max(stress_node, [], 'all');

dt=0.05; % Time Step ms
t=0:dt:12700000; %Time Array ms
t_on_dt = t(1,end)/dt;
```

```
V_f = zeros(C, t_on_dt+1);

for I_ST_loop = 1:C

% Constants and definitions

% Hogdkin Huxley constants
% Original Constants set for all Methods

Cnst_Cm= 1; % Membrane Capcitance uF/cm^2 Cm=0.01

VA = -50;
Cnst_ENa=55; % mv Na reversal potential
Cnst_EK=-72; % mv K reversal potential
Cnst_El=10; % mv Leakage reversal potential
Cnst_gbarNa=120; % mS/cm^2 Na conductance gbar Na=1.2
Cnst_gbarK=36; % mS/cm^2 K conductance gbar
Cnst_gbarl=0.3; % mS/cm^2 Leakage conductance gbarl
epsilon = 1.0;% from Shapiro and Lenherr 1972 epsilon varies between 1 and
10

V(1)= -60; % Initial Membrane voltage
REF_I=0.00; %External Current Applied

% parameters as per squid axon, taken from (Connor et al., 1977;Hille,
1992), Xu p227
GL = 0.3;
A_fac = 7;
B_fac = 7;
Cnst_gbarA = 47.7;
m_fac = 0.263;
h_fac = 0.263;
n_fac = 2.63;

% Declare variable arrays to save time
alpha_A = zeros(1,t_on_dt);
alpha_B = zeros(1,t_on_dt);
alpha_h = zeros(1,t_on_dt);
alpha_m = zeros(1,t_on_dt);
alpha_n = zeros(1,t_on_dt);

beta_A = zeros(1,t_on_dt);
beta_B = zeros(1,t_on_dt);
beta_h = zeros(1,t_on_dt);
beta_m = zeros(1,t_on_dt);
beta_n = zeros(1,t_on_dt);

A = zeros(1,t_on_dt+1);
B = zeros(1,t_on_dt+1);
h = zeros(1,t_on_dt+1);
m = zeros(1,t_on_dt+1);
n = zeros(1,t_on_dt+1);

%Variables
%===set the initial states===%
%V=-0; %Baseline voltage
alpha_n(1) = (1/n_fac) * (epsilon*(-.01 * ( (50+V) / (exp(-(V+50)/10)-1)
))); %Equation 12
beta_n(1) = (1/n_fac) * (epsilon*(.125*exp((-(V+60)/80)))); %Equation 13
```

```
alpha_m(1) = (1/m_fac) * (-0.1*( (V+35) / (exp(-(V+35)/10)-1))); %Equation
20
beta_m(1) = (1/m_fac) * (4*exp(-(V+60)/18)); %Equation 21
alpha_h(1) = (1/h_fac) * (0.07*exp(-(V+60)/20)); %Equation 23
beta_h(1) = (1/h_fac) * (1/(exp(-(V+30)/10)+1)); %Equation 24

%------------for Ik2------------------------------ Currents for 2nd
potassium channel, Xu p227
A_inf = ((0.0761*exp((V+94.22)/31.84))/(1+exp((V+1.17)/28.93)))^(1/3);
Ta_A = A_fac*(0.3632+(1.158/(1+exp((V+55.96)/20.12))));
alpha_A(1) = A_inf/Ta_A;
beta_A(1) = (1-A_inf)/Ta_A;

B_inf = (1/(1+exp((V+53.3)/14.54)))^4;
Ta_B = B_fac*(1.24+(2.678/(1+exp((V+50)/16.027))));
alpha_B(1) = B_inf/Ta_B;
beta_B(1) = (1-B_inf)/Ta_B;


A(1) = alpha_A/(alpha_A+beta_A);
B(1) = alpha_B/(alpha_B+beta_B);
%-----------------------------------------------

n(1) = alpha_n/(alpha_n+beta_n); %Equation 9
m(1) = alpha_m/(alpha_m+beta_m); %Equation 18
h(1) = alpha_h/(alpha_h+beta_h); %Equation 18


%Temperature related inputs for the Xu paper
Temp_noci = 55; % nociceptor temperature
Temp_thres = 43; % thermal pain threshold temperature
I_shift = -4; % -4 fudge factor introduced Xu to stop firing below
threshold value This influences the threshold of firing

Ch1 = 0.382; % constant for I_ST, frequency is proportional to this value
Ch2 = 0.064; % constant for I_ST, frequency is inversely proportional to
this value
Ch3 = 0.355;

Tn=[];
f =[];
f2=[];
f3=[];

k_temp = 3^((Temp_noci-6.3)/10);
k = 0.175; %This influences the rate of firing Range 0.03 to 0.15 is
reasonable

% I_ST = (Ch1*exp(((Temp_noci-Temp_thres)/Temp_thres)/Ch2)+Ch3)+ I_shift;
%Xu p231, I_st = stimulation current, eq 36
% as per Xu, I_ST = I_heat + I_chem + I_mech, where chem and mech are
assumed linear variables, p234

I_ST = zeros(t_on_dt,1);
time = zeros(1,t_on_dt);

    for i=1:t_on_dt % = t/dt = total amount of time steps
```

```
        I_ST = stress_node(i,I_ST_loop);

        time(i) = i;
        alpha_n(i) =  (1/n_fac) * (epsilon*(-.01 * ( (50+V(i)) / (exp(-
(V(i)+50)/10)-1) )));
        beta_n(i) = (1/n_fac) * ( epsilon*(.125*exp((-(V(i)+60)/80))));
        alpha_m(i) = (1/m_fac) * (-0.1*( (V(i)+35) / (exp(-(V(i)+35)/10)-1)
));
        beta_m(i) = (1/m_fac) * (4*exp(-(V(i)+60)/18));
        alpha_h(i) = (1/h_fac) * (0.07*exp(-(V(i)+60)/20));
        beta_h(i) = (1/h_fac) * (1/(exp(-(V(i)+30)/10)+1));

        %------------------------------for Ik2-------------------
        A_inf =
((0.0761*exp((V(i)+94.22)/31.84))/(1+exp((V(i)+1.17)/28.93)))^(1/3);
        Ta_A = A_fac*(0.3632+(1.158/(1+exp((V(i)+55.96)/20.12))));
        alpha_A(i) = A_inf/Ta_A;
        beta_A(i) = (1-A_inf)/Ta_A;

        B_inf = (1/(1+exp((V(i)+53.3)/14.54)))^4;
        Ta_B = B_fac*(1.24+(2.678/(1+exp((V(i)+50)/16.027))));
        alpha_B(i) = B_inf/Ta_B;
        beta_B(i) = (1-B_inf)/Ta_B;
        %------------------------------------------------------


        %---calculate the currents---%
        I_Na = (m(i)^3) * Cnst_gbarNa * h(i) * (V(i)-Cnst_ENa); %Equations
3 and 14
        I_K = (n(i)^4) * Cnst_gbarK * (V(i)-Cnst_EK); %Equations 4 and 6
        I_L = Cnst_gbarl *(V(i)-Cnst_El); %Equation 5
        I_k2 = Cnst_gbarA * (A(i)^3)* B(i) * (V(i) - VA); % not sure about
VA
        I_ion = I_ST - I_K - I_Na - I_L - I_k2;


        %---calculate the derivatives using Euler first order
approximation---%
        V(i+1) = V(i) + dt*I_ion/Cnst_Cm;
        n(i+1) = n(i) + dt*((alpha_n(i) *(1-n(i)) - beta_n(i) * n(i))*k);
%Equation 7
        m(i+1) = m(i) + dt*((alpha_m(i) *(1-m(i)) - beta_m(i) * m(i))*k);
%Equation 15
        h(i+1) = h(i) + dt*((alpha_h(i) *(1-h(i)) - beta_h(i) * h(i))*k);
%Equation 16



        A(i+1) = A(i) + dt*(alpha_A(i) *(1-A(i)) - beta_A(i) * A(i)); %for
Ik2
        B(i+1) = B(i) + dt*(alpha_B(i) *(1-B(i)) - beta_B(i) * B(i)); %for
Ik2
    end

    V_f(I_ST_loop,:) = V(1,:);
    f3 = f2;

    clearvars -except V_f f3 t dt t_on_dt M stress_node C
end
```

```
% V_f_added = (V_f(1,:) + V_f(2,:)); % Choose this for 2 nodes, etc.
% V_f_added = (V_f(1,:) + V_f(2,:) + V_f(3,:));
V_f_added = (V_f(1,:) + V_f(2,:) + V_f(3,:) + V_f(4,:) + V_f(5,:));
% V_f_added = (V_f(1,:) + V_f(2,:) + V_f(3,:) + V_f(4,:) + V_f(5,:) +
V_f(6,:) + V_f(7,:));

for i = 200000:200000:t_on_dt   %multi node voltage
    temp_peaks = findpeaks(V_f_added(1,i-199999:i),'MinPeakProminence',20);
    freq = (numel(temp_peaks)-1)/(10.0);
    f3 = [f3, freq];
end

% for i = 200000:200000:t_on_dt  %single node voltage
%     temp_peaks = findpeaks(V_f(1,i-199999:i),'MinPeakProminence',20);
%     freq = (numel(temp_peaks)-1)/(10.0);
%     f3 = [f3, freq];
% end

x_axis = 1: t(1,end)/10000;

x1 = 12:12:1270; %rms calcs
index = 12;
for i = 1:105
   y1(1,i) = rms(f3(1,index-11:index));
   index = index+12;
end

sample_index = 1; %stress calcs
for i=1:105
stress_sample(1,i) = stress_node(sample_index,1);
sample_index = sample_index + 2419000;
end

%%
% Plot the functions
figure;
hold on
a1 = plot(x_axis, f3); M1 = 'Node cluster A, f(Hz)';
a2 = plot(x1, y1); M2 = 'Node cluster A rms, f(Hz)';
a3 = plot(x1, stress_sample); M3 = 'Stress';
% ylim([0 60])
xlabel('time (10^1 seconds)');
ylabel('f(Hz)');
legend([a1;a2;a3], M1, M2, M3, 'Location','northwest')
hold off

figure;
plot(x_axis, f3);
% ylim([0 60])
xlabel('time (10^1 seconds)');
ylabel('f(Hz)');

% figure(2)
% plot(t,V_f(1,:));
% legend('Forward Euler');
% xlabel('Time (seconds)');
% ylabel('Voltage (mV)');
% title('Voltage Change for Hodgkin-Huxley Model');
```

```
figure;
plot(t,V_f_added(1,:));
legend('Forward Euler');
xlabel('Time (ms)');
ylabel('Voltage (mV)');
title('Voltage Change for Hodgkin-Huxley Model');

profile off; % Terminate profiler
profile viewer; % Display profiler data to indentify where code execution
is slowest
```

Appendix 3

```
%%%%%%%%%%%%%%%%%%%%%%%%%%%%%%%%%%%%%%%%%%%%%%%%%%%%%%%%%%%%%%%%%%%%%%%%%%%%
%%%%%%%%%%%%%%%%
%
% Harley Ewing 9704959
% Code to read FEBio stress vectors and plot them as pressure curves using
thin wall pressure vessel analysis
%
%%%%%%%%%%%%%%%%%%%%%%%%%%%%%%%%%%%%%%%%%%%%%%%%%%%%%%%%%%%%%%%%%%%%%%%%%%%%
%%%%%%%%%%%%%%%%


% Close and clear everything
clear;
clc;
close all;

profile on; % Initialise profiler to indentify where code execution is
slowest

%initialise constants
i = 0;
r = 2.88;

%initialise variables
pressure = zeros(100,1);
thickness = zeros(100,1);
time = 1:100;

filename = '50mmhg_stress_01.txt';
%filename = 'm_bladder_07_multistep_stress_N956.txt';

opts = detectImportOptions(filename);

preview(filename, opts);

t1 = readtable(filename, opts);

stress = table2array(t1(:,2));



filename = '50mmhg_displacement_01.txt';
%filename = 'm_bladder_07_multistep_disp_N956.txt';

opts = detectImportOptions(filename);

preview(filename, opts);

t2 = readtable(filename, opts);

displacement = table2array(t2(:,2:3));
```

```
% format long;

sz = size(stress); %Find size of array reported as "rows, columns".

C = sz(1,1);

%%%%% Use thin walled pressure vessel theory for inner pressure 2*t*sigma /
r = p
% t = thickness
% sigma = stress
% r = radius
% p = pressure


for i = 1 : C
    thickness (i,1) = displacement(i,1) - displacement(i,2);
end

for i = 1 : C
    radius (i,1) = (displacement(i,2) + displacement(i,1))/2;
end


for i = 1 : C
    pressure (i,1) = (2 * thickness(i,1) * stress(i,1)) /
((displacement(i,2) + r));
end

figure;
plot (time, pressure(:,1))
xlim([0 100])
xlabel('time (10^1 seconds)');
ylabel('Pressure (MPa)');

% fclose(fileID);

profile off; % Terminate profiler
%profile viewer; % Display profiler data to indentify where code execution
is slowest
```

Appendix 4

Table 7 – Bladder Inflation Data Wade Model

time at end of inflation (s)	infusion #	volume injected (uL)	total volume (uL)
0			76
200	1	100	176
800			
900	2	50	226
1500			
1600	3	50	276
2200			
2300	4	50	326
2900			
3000	5	50	376
3600			
3700	6	50	426
4300			
4400	7	50	476
5000			
5100	8	50	526
5700			
5800	9	50	576
6400			
6500	10	50	626
7100			
7200	11	50	676
7800			
7900	12	50	726
8500			
8600	13	50	776
9200			
9300	14	50	826
9900			
10000	15	50	876
10600			
10700	16	50	926
11300			
11400	17	50	976
12000			
12100	18	50	1026
12700			

Appendix 5

Secondary more complex mouse bladder mesh not incorporated into final research is shown in Figure 36. The more complex geometry of the second mesh was assigned a higher mesh density, and urethra and ureters.

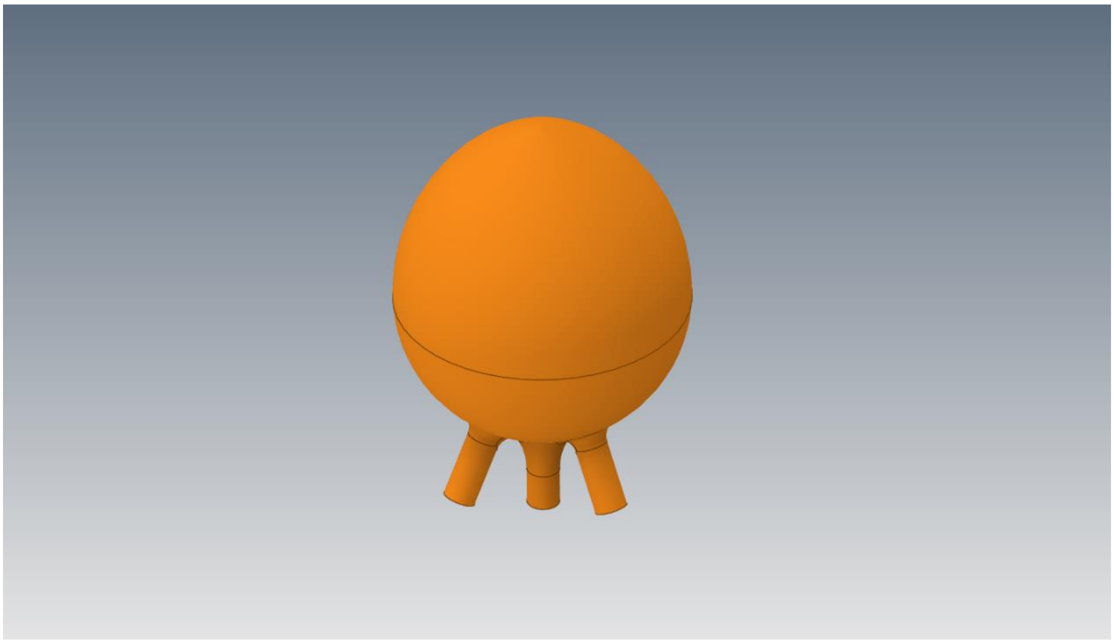

Figure 36 – Bladder mesh with ureters and urethra